THESIS FOR THE DEGREE OF LICENTIATE OF ENGINEERING

Across the drip-line and back: examining ^{16}B

Developments for and analysis of experiments with the LAND/R^{3}B setup

RONJA THIES

Department of Fundamental Physics
CHALMERS UNIVERSITY OF TECHNOLOGY
Göteborg, Sweden 2014

Across the drip-line and back: examining ^{16}B
Developments for and analysis of experiments with the LAND/R^{3}B setup
RONJA THIES

Department of Fundamental Physics
Chalmers University of Technology
SE-412 96 Göteborg
Sweden
Telephone: +46 (0)31-772 10 00

Cover:
A compilation of plots which are part of this work. All can be found in the thesis.

Chalmers Reproservice
Göteborg, Sweden 2014

Across the drip-line and back: examining ^{16}B
Developments for and analysis of experiments with the LAND/R^{3}B setup
RONJA THIES
Department of Fundamental Physics
Chalmers University of Technology

Abstract

Until today, after about one century of research, the atomic nucleus, a basic building block of nature, is still a fascinating puzzle. The field of nuclear physics strives for a better understanding employing both experimental and theoretical efforts. To gain further knowledge, nuclear physics experiments grow more and more sophisticated, pushing the limits of feasibility. Nuclei beyond the drip-lines are a target believed to supply information about the nuclear interaction which is not accessible otherwise.
High-energy nuclear reactions are versatile tool to study nuclei at and beyond the drip-lines. One of the world-leading experimental-setups for high energy nuclear reactions is the LAND/R^{3}B setup at GSI which offers excellent opportunities to study exotic nuclei close to and beyond the drip-lines.

The present work centers around the study of the unbound nucleus ^{16}B, analyzing an experiment performed at the LAND/R^{3}B setup. ^{16}B is the lightest unbound boron isotope, while heavier bound boron isotopes exist. It is studied by quasi-free scattering, produced by ^{17}C undergoing a (p,2p) reaction, which is the production mechanism leaving the produced fragment least disturbed.
The relative energy, transverse momentum distributions, and momentum profile of the ^{16}B system are presented. At the current stage of analysis, relative energy and transverse momentum distributions are in agreement with previous measurements. A momentum profile has not been extracted before.
Due to the nature of these experiments trying to push the frontier, developments of experimental techniques are an integral part of research. A significant share of this work is dedicated to developments, enabling or facilitating the analysis of the present and other experiments performed with the same setup.

Keywords:
Neutron-dripline, Unbound Nuclei, Analysis, Calibrations, Radioactive Beams, Simulations, R^{3}B, GSI, FAIR

Contents

1 Introduction

In 2013 the number of atomic nuclei which had been experimentally observed was 3847 [1]. Of these only 254 are stable[1)] and more isotopes are discovered every year. Stable nuclei are a prerequisite for atoms, which are a prerequisite for molecules, and so forth. Why are certain nuclei stable and others are not? One would expect that something this fundamental to our life is well understood. It is not. There exists no theoretical description which is able to describe the interaction of the constituents of the nucleus, protons and neutrons, such that all properties of all nuclei can be derived from it. As a consequence we also do not know in detail how the almost 300 nuclei abundant on Earth are formed in the cosmos.
The problem is that so far nobody has been able to derive the nucleon-nucleon interaction from first principles. It is the residual of the strong interaction at the length scale of nuclei – femtometer. To day the best approximations work with a potential created by the nucleons comprising e.g. spin-orbit coupling, tensor and 3-body components.
The first theory to successfully describe the properties of a large number of atomic nuclei is the shell model developed by Goeppert-Mayer and Jensen in the 1950s [2–5]. It was developed in order to explain the "magic numbers", which describe the number of protons (neutrons) after which the separation energy[2)] drops sharply while it otherwise changes monotonically with the number of protons (neutrons). The nuclear shell model uses a mean-field approach; it assumes an average potential created by the nucleons which the potential actually acts on. It is very successful but works unfortunately only close to magic numbers, i.e. shell closures, and not very far from

[1] Those 254 have never been observed to decay.
[2] The separation energy regarded here is the energy it takes to remove two nucleons (same isospin). The fact that two nucleons have to be removed is due to pairing otherwise obfuscating this clear trend.

the line of stability. It is still actively developed to take increasingly complicated interactions into account, but is limited by computational power [6, 7].
As a consequence other theories were developed. Examples of these theories are the Nilsson model, "ab-initio"-methods, other mean field approaches and density functional theories. Each of these has a region in the nuclear landscape in which they are successful, but none is able to describe the full picture. All of them use the terminology of the nuclear shell model.
Understanding the nuclear force means being able to calculate for example masses, charge distributions and reaction rates, i.e. being able to predict the nuclear structure. This is important in order to be able to understand the formation of nuclei in astrophysical processes (in stars, in supernovae, in the big bang...). This does not include the stable nuclei only, but especially exotic[3)] nuclei, as many of them lie on the path of forming a stable heavier nucleus. These nuclei are also crucial to understand the evolution of nuclear structure from stable to unbound and as a testing-ground for nuclear theories.
When approaching the drip-lines[4)] from the stable domains, severe changes in the structure of these increasingly exotic nuclei can be observed, due to the importance of different components of the interaction changing. This can be observed for example by the formation of halos in light nuclei at the drip-lines, recently summarized in Refs. [8, 9]. Another severe effect is the shifting of magic numbers when approaching the drip-lines, summarized e.g. in Ref. [10]. And this might not yet be the full picture.
Crossing the drip-line towards unbound nuclei, it is possible to learn more about the transition from bound to free systems. The previously closed quantum system becomes open and the mean-field approximations reach their limits. Thus, the unbound nuclei present yet another picture of the nucleon-nucleon interaction, being able to supply information bound systems cannot deliver and due to that constitute another crucial part for the understanding of the nuclear force.

[3]Exotic nuclei is another expression for unstable nuclei. The further away from stability an isotope is, the more exotic it is considered to be.
[4]The drip-line is the name of the "border" between bound and unbound nuclei. It exists on the proton-rich and on the neutron-rich side of the chart of nucleides, called the proton drip-line and the neutron drip-line respectively.

These nuclei far from the valley of stability have just rather recently become available at radioactive ion beam facilities and push the limits of both experimental and theoretical physics. Unbound nuclei can be created via e.g. knock-out[5)] of single nucleons from nuclei at the drip-lines. More about the production can be found in Sec. 1.2.
The focus of this work is the unbound nucleus ^{16}B produced from ^{17}C and the following section summarizes the available information about it.

1.1 The ^{16}B isotope

In 1974 Bowman *et al.* [11] demonstrated experimentally that ^{16}B is unbound. This was shown by spallation of uranium with a 4.8 GeV proton beam, observing ^{15}B and ^{17}B, but not ^{16}B. An experiment at GANIL using fragmentation of ^{40}Ar on a tantalum target at 44 *A*MeV [12] confirms this.
Bohlen *et al.* derived a mass excess of 37.08(6) MeV, coming to the conclusion that ^{16}B is unbound by only 40(60) keV [13] using the transfer reaction $^{14}\mathrm{C}(^{14}\mathrm{C},^{12}\mathrm{N})^{16}\mathrm{B}$ with about 335 MeV beam energy at HMI in 1995. Further analysis of the experiment in Ref. [13] determines a second state at 2.32(7) MeV above the particle threshold and assigns the previously found state tentatively to the ground state[14]. For both states the authors present differential cross sections and a width[6)].
There are several experiments which use proton removal from ^{17}C at energies below 100 *A*MeV. Fragmentation of a 52 *A*MeV ^{17}C beam on a C target at MSU was used to determine an upper limit of the lifetime of ^{16}B at 191 ps (68% CL) [16]. Referring to the shell model, the authors tentatively assume that the last neutron occupies a $d_{5/2}$ orbit in the ground state of ^{16}B, concluding that the expected lifetime is of the order of 10^{-16} s in case of 10 keV decay energy.
A further experiment at GANIL employing proton knock-out from ^{17}C at 35 *A*MeV on a carbon target confirms a low lying state, though it places it at 85(15) keV above

5) When two nucleons collide and in one of them one nucleon is removed and does not attach to the other nucleus, but leaves the collision point, this is called knock-out of that nucleon.

6) The g.s. is assigned an upper limit of 100 keV in width and the excited state is reported to have a width of 150 keV.

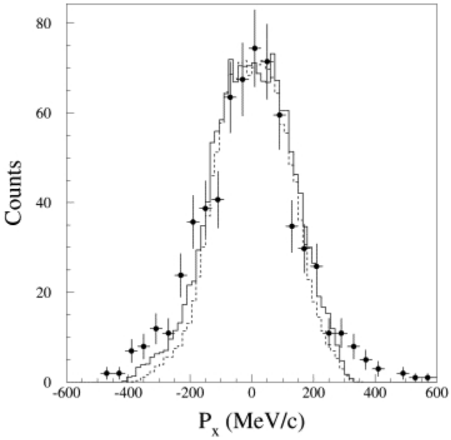

Figure 1.1: The transverse momentum measured by Ref. [15]. Dots indicate the measured data and the lines show two different calculations using a p-wave proton, using the sudden approximation (solid) and an Eikonal type calculation (dashed). For details see Ref. [15].

particle threshold using a d-wave fit to the measured relative energy spectrum [15]. Ref. [15] also reports the transverse momentum distribution shown in Fig. 1.1 without reporting its width. Further measurements at MSU using a beam of 55 *A*MeV ^{17}C impinging onto a Be target find a resonance at 60(20) keV, in agreement with both previous measurements [17].
Except for the shell model calculations [18], also microscopic cluster calculations have been performed [19]. The theoretical predictions, as well as the experimental results from Ref. [14] and Ref. [15] are shown in Fig. 1.2.

1.2 Nuclear Physics Experiments

Studying unstable atomic nuclei is not a straightforward business. Unstable nuclei need to be created first and need to be transported to the experiment rather quickly (depending on the lifetime, ms to ns). This is solved by creating beams of these exotic nuclei. There are two main types of creating exotic nuclei: in-flight production,

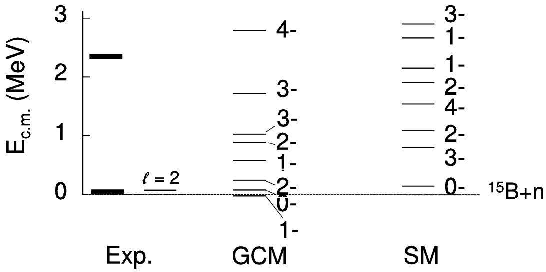

Figure 1.2: Figure illustrating the different levels measured (Exp.) by Ref. [14, 15], calculated in the GCM model (GCM) [19] and calculated within a shell-model approach (SM) [18]. Figure taken from Ref. [19].

as used in this work, and post-acceleration used in ISOL-type facilities. A recent review of radioactive ion beam production and facilities is given in Ref. [20].

In-flight production utilizes a beam of a stable isotope which is accelerated to (from medium up to) relativistic energies and brought to collide with a target, so that all kinds of different nuclear reactions take place. The type of reaction depends on the impact parameter[7)], which cannot be controlled at the size of nuclear collisions. There are mainly three types of reactions used for creating exotic nuclei, fragmentation, spallation and fission. In a fragmentation reaction, part of the nucleons are removed from the projectile nucleus due to the interaction with a target nucleus. The rest of the projectile, the spectator part, does not interact with the target nucleus. Therefore this part often stays intact after the collisions (a few nucleons usually evaporate) and does, to a good approximation, not loose kinetic energy, as illustrated in Fig. 1.3. This reaction is very useful to produce neutron-rich, light nuclei, because the neutron to proton ratio is kept approximately constant in this reaction[8)] and heavier stable nuclei have a higher neutron to proton ratio, but also because it creates a spread in the neutron to proton ratio without disturbing the reaction products (in a first approximation).

[7]The impact parameter is defined as the distance between the centers of mass at the point of closest approach of two particles, perpendicular to the initial direction of motion of the object.

[8] That concerns the collision, the evaporation changes that.

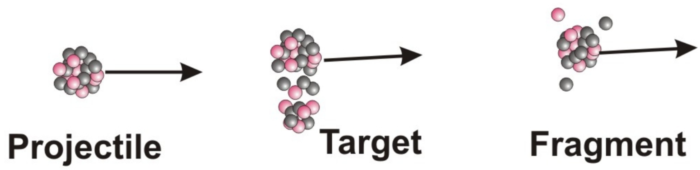

Figure 1.3: Illustration of a fragmentation reaction. Picture from T. Nilsson [21].

Unbound nuclei require production at the detector setup as they decay immediately[9]. Therefore beams with nuclei at the driplines are often used to produce unbound nuclei using knock-out or transfer reactions. In transfer reactions one nucleon looses one (up to a few) nucleons to the other nucleus. In knock-out reactions the collision of two nuclei (A and B) leads to one (up to a few) nucleons leaving e.g. nucleus A and not attaching to nucleus B. This nucleon(s) is regarded to have been knocked-out from nucleus A. The knock-out reactions are more likely at higher relative energies. Both reactions can be used to study unbound nuclei, knock-out reactions though, are a versatile tool for spectroscopy, as they remove one nucleon (cluster) from the nucleus, approximately not interacting with the rest of it. One proton knock-out reactions are the tool chosen to study ^{16}B in this work. Cross-sections for these reactions are quite low (on the order of mb).
Generally, also beam intensities of exotic nuclei are low, down to a few ions per second (depending heavily on isotope and production mechanism). It is therefore important that angular coverage and efficiency of detectors are as high as possible[10]. Striving for measuring in complete kinematics[11] which allows better reconstruction and selection of a reaction channel, the granularity of the detectors increases as well as their number. These two facts lead to an increasing amount of detector channels, requiring more advanced read-out and analysis. The setup used in this work features 13 detectors and in the order of 10000 (electronic) read-out channels. The facility

[9] As seen in the previous subsection immediately usually means on the order of ps or smaller. Resonances can enhance the lifetime of such an unbound system.
[10] In principle also the time of measurement could be increased, but beam time is scarce and expensive, and angular coverage adds also to the information available.
[11] This means all particles and their 4-momentum vectors are determined.

and the detector setup which are used in this work are explained in the following Chapter.

1.3 Outline of the thesis

The thesis is structured in the following way: Ch. 2 introduces the experimental facility and the setup used in this work. Thereafter in Ch. 3 the software which was employed is briefly introduced. The calibration the experimental setup is described in Ch. 4. The developments which were performed by the author during this work, mainly concerning calibration, are separately discussed in Ch. 5. Ch. 6 presents the results obtained so far in this project. The concluding Ch. 7 contains the conclusions and outlook of this work. Any acronym used in this work should be found in the Glossary at the end of this thesis.

2 Experimental Setup

2.1 Experimental facility and beam production

The experiments were, as mentioned, performed at the GSI Helmholtzzentrum für Schwerionenforschung (GSI Helmholtz Facility for Heavy Ion Research) in Darmstadt, Germany. A sketch of the facility is shown in Fig. 2.1, in which also the LAND/R^{3}B setup at which the experiment was conducted is indicated. The LAND/R^{3}B setup is the transitional setup from the LAND setup, which was named after the neutron detector LAND (which is still in use in the setup), to the R^{3}B (Reactions with Relativistic Radioactive Beams) setup at FAIR. FAIR (Facility for Anti-proton and Ion Research) is the international successor facility of the (previously national) GSI facility. FAIR will among other improvements and new experiments allow for higher beam energies and higher luminosities. For a detailed description of the facility see Ref. [22]. The R^{3}B setup will be adjusted to higher beam energies and luminosities, while also improving resolution. The present setup thus not only serves for physics research, but also as a prototype for the next generation experimental setup R^{3}B. In the following the process of creating radioactive ion beams for the experimental setup is described.

Ions are extracted from the ion source, bunched and accelerated in the UNILAC up to energies of 11.4 AMeV (for Uranium). For experiments at lower energies the beam can be sent to the first experimental hall after the UNILAC. In order to create radioactive ions, the beam needs to be accelerated further and is thus injected into the SIS18, a synchrotron being able to accelerate ions up to energies of 4.5 AGeV (for protons; smaller charge to mass ratios result in lower energies). From the SIS18, the relativistic ions can be extracted and sent directly to the ESR (experimental storage

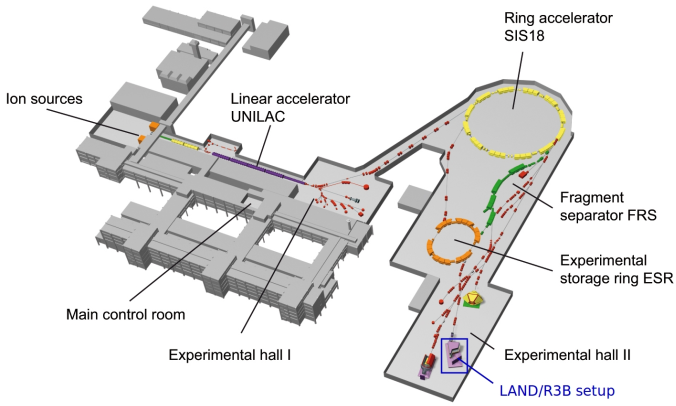

Figure 2.1: Sketch of the present GSI facility. Important parts for beam production are the ion sources, the UNILAC (universal linear accelerator), the SIS18 (Schwerionen Synchrotron, heavy ion synchrotron) and the FRS (fragment separator). The experimental site of the experiment is marked in blue. Figure is not to scale.

ring) and the experimental setups in the second experimental hall, but in order to create radioactive ions the beam needs to be guided to the FRS. A schematic drawing of the FRS is shown in Fig. 2.2.

At the FRS, the beam impinges onto a primary target, which is usually light and thick, and undergoes reactions like fragmentation, producing all possible lighter ions. Since it is not possible to control the reactions such that only the ion(s) of interest are produced[1)], these have to be separated from uninteresting products after production. This is done after the primary target using the "$B\rho$ - ΔE - $B\rho$" technique. The term $B\rho$ is the magnetic rigidity and defined as $B\rho = \frac{p}{q}$ where B is the (magnitude of the) magnetic field, ρ is the cyclotron radius[2)], p is (the magnitude of the) momentum of the ion, and q the charge of it. This selection requires that a specific energy

[1]The choice of primary beam, production target and beam energy can be optimized in order to maximize the yield, though.

[2]The cyclotron radius is defined as: $\rho = \frac{mv_\perp}{|q|B}$ with m being mass and q charge of the ion, B the magnitude of the magnetic field and $v_\perp$ the velocity component of the ion perpendicular to the field.

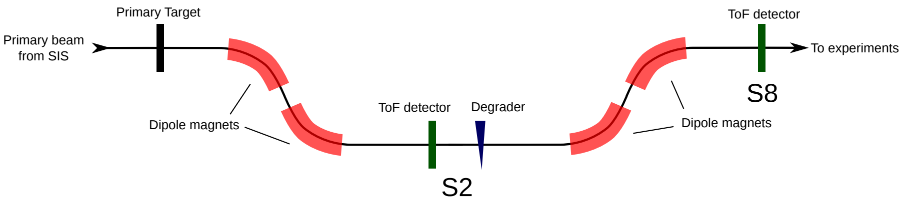

Figure 2.2: Schematic drawing of the FRS, focusing on the working principle. Beam steering and monitoring devices are not indicated. This drawing is not to scale.

range is chosen[3)] since the magnetic rigidity and energy loss depend on it. First the ions are selected by their magnetic rigidity using the magnets indicated in Fig. 2.2. Since the rigidity implies only a mass over charge ratio selection (for a given beam energy), this is not sufficient. Therefore, the beam passes a degrader[4)]. Since ions loose energy proportional to their charge squared, this splits the energies of the ions up according to their charge. The second selection on magnetic rigidity, together with the previous two stages, results into a selection according to mass and charge (and kinetic energy).

After the ions of interest have been selected, they are guided to the experimental setup, in the current case to Cave C[5)].

In the present experiment, the S393 experiment, a primary beam of ^{40}Ar at an energy of 490 AMeV was used together with a production target of 4 g/cm^2 Be for radioactive beam production.

2.2 Detector Setup

The LAND/R^{3}B setup is a setup for complete kinematics experiments of nuclear reactions using relativistic radioactive ion beams. Reaction products are detected one-by-one and often in several detectors, which allows for event-by-event data collection and reconstruction. A sketch of the full setup is shown in Fig. 2.3 and the

[3] As mentioned in the introduction, fragmentation reactions lead to almost no energy loss, thus the energy window is situated close to the unreacted beam energy.
[4] Since a light cocktail beam was wanted in S393 no other degrader than the ToF detector was used.
[5] There are several other setups it can be guided to.

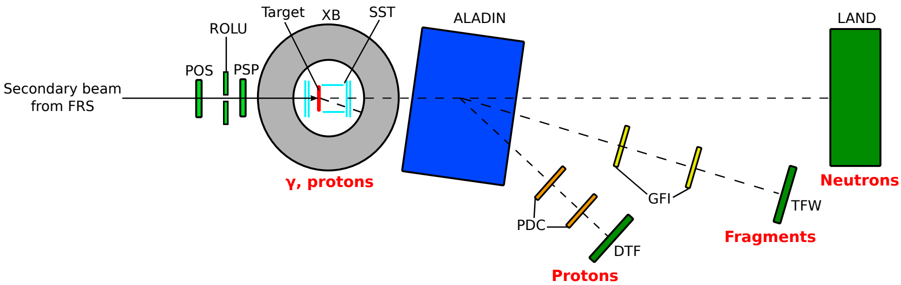

Figure 2.3: Sketch of the LAND/R^{3}B setup for the S393 experiment, not to scale. The ions from the FRS come from the left and impinge onto the reaction target(depicted in red). Surrounding detectors and detectors behind the magnet detect the reaction products. For a detailed description see text.

detectors as well as their acronyms are described in the following subsections.
The incoming ions are identified using the time-of-flight (ToF) between start- and stop-detector POS and detectors at the FRS (located at the focal points S8 or S2) and the energy deposit in the PSP. Their direction is usually inferred from the two SST detectors before the target. The SST detectors behind the target determine the position and therefore also angle of the outgoing fragment. The surrounding Crystal Ball (XB) detects emitted gammas as well as protons and neutrons scattered at large angles ($> 7.5°$).
All particles that leave the Crystal Ball in the forward direction enter into ALADiN, a large acceptance dipole magnet, bending and therefore separating the particles according to their magnetic rigidity. Neutrons, since they are uncharged, pass undisturbed through the magnetic field and are detected in the neutron detector LAND. Ions heavier than protons (i.e. $^A/_Z > 1$) will be bent to angles around $17°$. Their position in the horizontal direction perpendicular to the beam (x-direction) is detected in the GFI detectors, and their ToF and (rough) position is detected in the TFW detector. The PDCs detect the position of the stronger bent protons and the DTF gives the ToF and rough position of the protons.

2.2.1 Incoming beam

Incoming beam detectors are all detectors upstream of the target, used for identification and characterization of the incoming beam. Two detectors are located at the FRS, at the focal points S2 and S8. These detectors are called SCI1 and SCI2 respectively. They are made of thin sheets of plastic scintillator with PMTs at two sides (left and right). These detectors are solely used for ToF determination[6]. During the S393 experiment the SCI1 detector did not work.

The POS (position detector), is a quadratic sheet of plastic scintillator with light-guides and PMT at all four sides (see Fig. 2.4), which, in contrast to its name, is used solely as start and stop detector for ToF measurements. Its resolution in the present experiment is σ=470 ps, depending on beam energy and ion species. The ROLU is an active veto detector which can be used to decrease the beam spot size of the recorded ions. Its opening, i.e. allowed region for ions to pass without being vetoed is adjustable. If the ROLU detects a particle, a trigger is sent to the central trigger logic indicating that an ion hit the ROLU. The central trigger logic is configured such that those events are not recorded. The PSP (position-sensitive PIN-diode), also situated in front of the target area, is used for charge identification by measuring the deposited energy via the cathode read-out. It is in principle also capable of position detection, with the use of the four anode read-outs situated in the corners. This is difficult due to the relatively poor resolution for the low-Z ions used

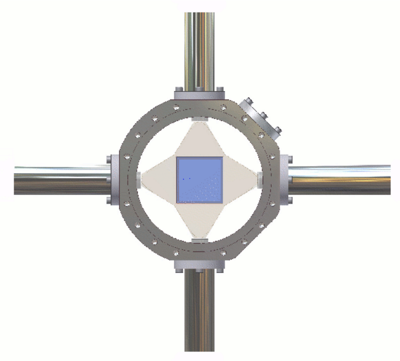

Figure 2.4: Illustration of the POS detector. The blue square indicates the active area and the gray shaded area depicts the light guide material. The holding flange and PMT flanges are indicated. Picture taken from Ref. [23].

[6] Both between SCI1 and SCI2, but also between SCI1 (SCI2) and POS.

in the present experiment, but has recently been shown possible [24].

2.2.2 Detectors surrounding the target

The SST (silicon strip detector) detectors surround the target area. Two are situated perpendicular to the beam in front of the target and two perpendicular to the beam behind the target. Four units form a box around the beam directly behind the target, between the latter and the two inbeam SSTs. The SSTs are 300 μm thick double sided silicon strip detectors delivering position information in both dimensions of the detector. They have a pitch size of 27.5 μm on the S-side (vertical strips), only every 4^{th} channel is read-out, the others are capacitively coupled, thus having a read-out pitch of 110 μm. The K-side (horizontal strips) has a pitch of 104 μm and every channel is read out. Energy measurements are also possible. The two inbeam SSTs in front of the target are used to determine the direction of the incoming ion, whereas the two behind the target are used to derive the direction of the outgoing beam. The box of SSTs is used to infer directions of charged particles scattered at large angles. The SSTs behind the target can be seen in green in Fig. 2.5 showing a sketch of the target area. One half of the first inbeam SST in front of the target was not functioning during the experiment. The position resolution is 50 μm on both sides of the SST detectors.

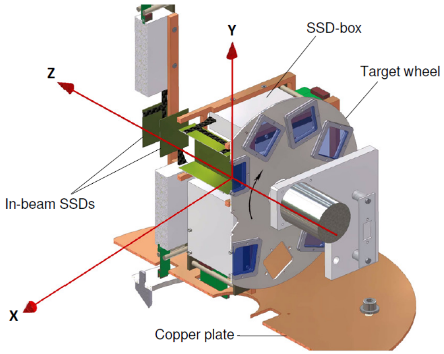

Figure 2.5: Illustration of the target area. The targets (blue) mounted on the target wheel can be seen. The SST detectors behind the target are drawn in green. The coordinate system used in the Cave is indicated, and will be the used coordinate system in this thesis unless indicated otherwise. Figure taken from Ref. [25].

The Crystal Ball detector surrounds the target and the SST detectors. It is a spherical

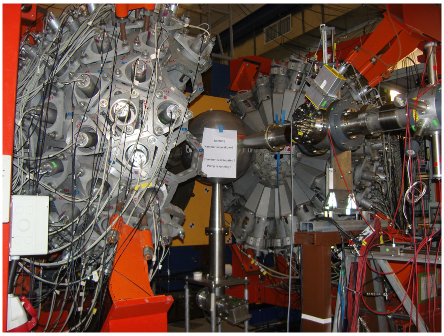

(a) Photo of the opened Crystal Ball with target chamber inside. Parts of the POS detector can be seen at the very right of the picture.

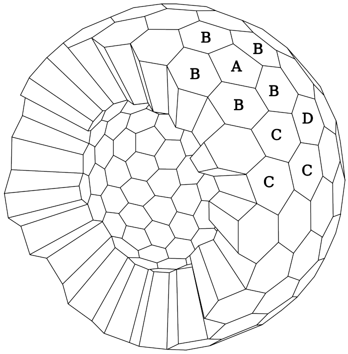

(b) Sketch of a part of the Crystal Ball. The letters indicate the different crystal shapes and their arrangement.

Figure 2.6: Figures illustrating the Crystal Ball detector.

shell of 162 NaI(Tl) crystals of 20 cm length outside an inner radius of 25 cm. It was originally constructed as a calorimeter for gamma rays for stopped beam experiments in the 80s [26] and is presently used to detect gammas as well as protons and neutrons scattered at large angles. In order to handle this large range of deposited energy, the PMT of the 64 most forward crystals are read out additionally at a lower gain stage, providing a high-energy range read-out, allowing for proton (and neutron) energy detection. A photograph of the detector is shown in Fig. 2.6a, and a sketch of it is shown in Fig. 2.6b, where the four different crystal shapes and their arrangement is indicated. As can be seen, there are three different hexagonal shapes and one pentagonal shape. The angular resolution of the detector is limited by the granularity to a 7.5° uncertainty, and the energy resolution of the low-energy branch is 6%.

2.2.3 Neutron detector

The neutron detector LAND (large area neutron detector), located about 12.4 m behind the target (front face of the detector), has a front face area of 2x2 m^2 and is one meter deep. It is constructed out of 10 planes which in turn are built out of 20 paddles each. A paddle consists of several layers of iron and plastic scintillator and has the dimensions 10x10x200 cm^3. Each paddle has two PMTs for read out at its far ends, which stick out left and right or top and bottom, depending on the orientation of the plane. The planes are arranged such that the paddles in one plane are perpendicular to the paddles in the adjacent planes. The neutrons themselves do not excite the scintillator material, but only the charged products of an interaction of a neutron with an atomic nucleus. This is why iron was introduced, in order to increase the interaction cross section of neutrons. The sandwich construction of iron and scintillator is supposed to enable detection of most charged particles created in the iron. The crossing paddle construction allows for a good position resolution in both dimensions, as a paddle has only a good spatial resolution along its length. Therefore LAND works both as a ToF detector and as a position-sensitive detector for the interactions of detected neutrons. The intrinsic time resolution of LAND is usually around 370 ps and the spatial resolution is ca. 5 cm [27].

2.2.4 Fragment arm detectors

After bending the fragments in the magnet it is crucial to detect them with a sufficient position resolution in the dispersive (x-)direction to achieve an adequate mass resolution ($\sigma \leqq 0.25$ mass units). This is the purpose of the GFI (Grosser Fiber Detektor, big fiber detector) detectors. A GFI detector has a cross sectional area of 50x50 cm^2 and is made of 475 fibers, 1x1 mm^2 thin. The fibers are connected to a position sensitive PMT on one end, and a normal PMT at the other end, yielding position and timing information respectively. The position resolution is $\sigma = 650\mu$m [28].

The TFW (ToF Wand, ToF wall) is situated at the end of the fragment arm, about 11 m from the target. It is made of 18 vertical and 14 horizontal plastic scintillator paddles, all 10 cm wide and 6.5 cm thick. Each paddle is read out by a PMT at both of its far ends, giving a good timing information for ToF measurements (around 0.5 ns resolution), but also a position information with a resolution of about 5 cm. A photograph of the detector can be seen in Fig. 2.9.

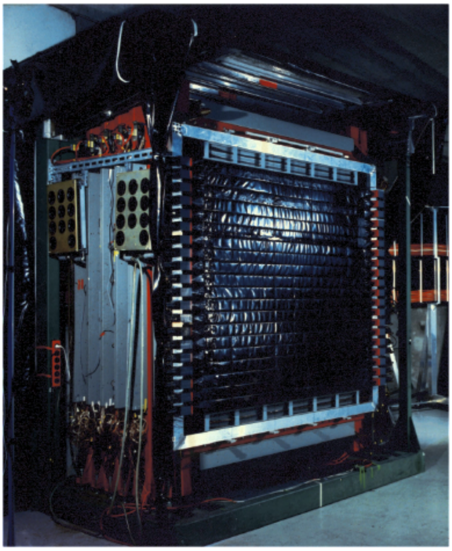

Figure 2.7: Photograph of the LAND detector with the cover opened. Picture taken from Ref. [23].

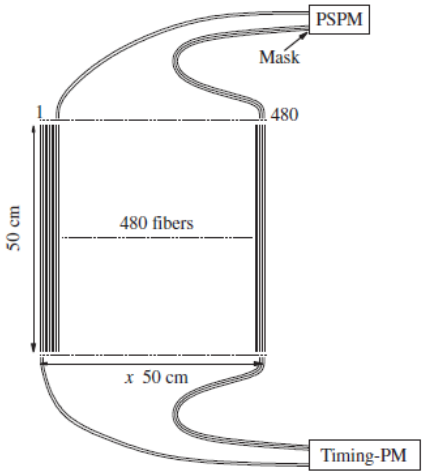

Figure 2.8: Sketch of the GFI layout. Picture taken from Ref. [28].

Figure 2.9: Photo of the TFW. Taken from Ref. [23].

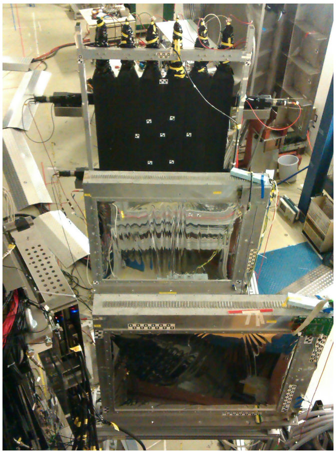

Figure 2.10: Photo of the proton arm detectors during the S412 experiment. Detectors but not the positions are the same as in the S393 experiment. The central horizontal paddle it not mounted, and the PDCs are not gas-filled in the photo.

2.2.5 Proton arm detectors

Protons scattered at small angles (below 7.5°) or emitted from the fragment are detected in the Proton arm. It consists of the two PDCs (proton drift chambers) and the DTF (Dicke ToF Wand, thick ToF wall). The PDCs are gas-filled detectors with an active area of 100x80 cm^2. They consist of 112 horizontal and 144 vertical wires arranged in a hexagonal double-layer pattern with a "diameter" of 16 mm. The position resolution in the present experiment is 0.35 mm for both detectors in x and y directions[29]. The DTF is made of 9 plastic scintillator paddles, 6 vertical and 3 horizontal. The vertical paddles create an active area of 120x120 cm^2 and are 1.5 cm thick. The horizontal paddles are 10.4 cm wide and only used for calibration purposes. They are positioned in the centre, on top and bottom behind the vertical paddles, as can be seen in Fig. 2.10.

2.3 Data acquisition

So far the set-up with its purpose and the different detectors have been explained. The signals of the detectors have to be collected and stored for later analysis. The original signal from a detector channel usually carries time and energy information (not all detectors yield energy information). The analog electric signal from a channel needs to be treated differently in order to extract the time or the energy information. To store the energy information, the integral of the pulse is to be extracted, as it is proportional to the deposited energy. Usually a QDC (charge to digital converter) is used, sometimes also an ADC in combination with a shaper/amplifier, and the digital value is stored in list-mode files. In order to store the time information, the timing of the pulse needs to be extracted, which is usually done with a TDC (yielding a time versus Master Start). Also this information is stored in the list-mode files. In order for the electronic modules to convert an energy, or measure the time, they need the information that they are supposed to do so. This information is provided by the central trigger logic.

2.3.1 Trigger

In order for the DAQ (data acquisition) to decide what events are supposed to be processed and stored, a trigger system is necessary[7)]. The trigger tells different modules that an interesting information is coming, should be processed and sent to the DAQ. So the trigger needs to convey information about the signals to arrive. This is realized such that signals for trigger production are processed immediately, while signals conveying other information are delayed. Most of the detectors in the set-up generate a so-called raw trigger. This is a logic signal conveying the information that the specific detector detected something which may be worth saving. These triggers are processed in the central trigger-logic which generates the master start (master trigger).

A summary of the raw triggers is found in Table 2.1. The central trigger logic

[7] This is not completely correct. So-called “triggerless” systems exist. There data from different detector channels are collected independently of the other channels. Still internally this detector needs some kind of trigger decision for each channel.

1 POS!ROLU	as 2 but no signal in ROLU allowed
2 POS	signal in at least 2 channels of POS above threshold
3 land mult.	requirement that at least 2 channels are above threshold
4 land cosm.	requirement that at least 4 channels are above threshold
5 TFW	at least 2 channels must be above threshold
6 TFW del.	same as 5, but delayed
7 DTF	at least 2 channels must be above threshold
8 DTF del.	same as 6, but delayed
9 XB or	at least one PMT fired above threshold
10 XB or del.	same as 9, but delayed
11 XB sum	at least one high-energy deposit in the full XB
12 XB sum del.	same as 11, but delayed
13 S8	one channel over threshold, only for self-triggering
14 PIX	signal over threshold
15 NTF	trigger for a detector which was only tested
16 XB L+R	at least one high-energy deposit in both left and right half of the XB
aux 1	beam on - signal from SIS marking the beam pulse
aux 2	early pile up - stretched and delayed POS, such that ions coming too close in time can be vetoed
aux 3	late trigger kill - stretched and delayed POS, such that it starts when QDC and TDC of POS are out of range

Table 2.1: List of the raw triggers used in S393. The requirement for the trigger to be generated is summarized. More details can be found in Ref. [23].

raw trig. / Tpat	1	3	5	6	7	11	13	14	aux 1	aux	aux 3
1 Min. Bias	x	-	-	-	-	-	-	-	x	-	-
2 Fragment	x	-	x	-	-	-	-	-	x	a	-
3 FRS S8	-	-	-	-	-	-	x	-	x	-	-
4 XB sum	x	-	x	-	-	x	-	-	x	a	a
5 Proton	x	-	x	-	x	-	x	-	x	a	-
6 GB - pileup	x	-	-	-	-	-	-	-	x	a	-
7 Pix	x	-	-	-	-	-	-	x	x	-	-
8 Neutron	x	x	x	-	-	-	-	-	x	a	-

Table 2.2: Table indicating which raw triggers have to be present in order to generate certain trigger patterns for inspill data collection. The generated Tpats are listed in the first column and the needed raw triggers indicated by an “x” in the respective columns. An “a” indicates an anti-coincidence requirement and “-” indicates no requirement.

generates coincidences between the different triggers arriving, and on the basis of these coincidences decides whether data is to be stored or not (i.e. a master start sent or not). When a trigger is accepted the combination of raw triggers leading to the positive trigger decision are stored in the so called “trigger pattern”, Tpat, uniquely identifying the combination. To generate the Tpats one discriminates between inspill and offspill triggers. Inspill are triggers which arrive when the beam arrives at the cave. These triggers are important to filter out events which are interesting for physics analysis. Offspill triggers are those generated when no beam entered the cave[8)]. These triggers are caused by background radiation, and are extremely important for calibration and monitoring of the detectors. The generated inspill trigger patterns are summarized in Table 2.2. A neutron trigger event does e.g. require an ion in the cave (POS!ROLU), that the corresponding fragment is detected (TFW), of course that a neutron is detected (land mult.) and that no pileup is present (aux 2). An offspill trigger pattern usually only requires one detector and that no beam is arriving (anti-coincidence). The offspill trigger patterns and which raw triggers they require are summarized in Table 2.3.

[8]Due to the synchrotron the beam is not continuous, but bunched. Therefore there are always (short) time periods when no beam arrives at the setup, though beam is taken in general.

Tpat \ raw trig.	1	4	6	8	10	12	16	aux 1
9 XB muon	a	-	-	-	-	x	-	a
10 LAND cosm.	a	x	-	-	-	-	-	a
11 TFW cosm.	a	-	x	-	-	-	-	a
12 XB gamma	a	-	-	-	x	-	-	a
13 DTF cosm.	a	-	-	x	-	-	-	a
15 XB L+R cosm.	a	-	-	-	-	-	x	a

Table 2.3: Table indicating which raw triggers have to be present in order to generate certain offspill trigger-patterns (for data collection). The generated Tpats are listed in the first column and the needed raw triggers indicated by an "x" in the respective columns. An "a" indicates an anti-coincidence requirement and "-" indicates no requirement.

As the vast majority of ions does not interact in the target, very few events are actually of interest later on for physics. Since every recording causes dead-time[9)] it is in general not possible to take every trigger with the presented setup. Triggers for calibration (e.g. Pix) and normalization (e.g. min. bias) are usually not all taken, but handled by downscale factors. A downscale factor of n for a certain Tpat leads to only every n^{th} of this Tpat being collected and saved. Thus the downscale factors should be chosen in order to minimize the statistical error induced. For cross section deductions for example, usually data from one reaction trigger as well as data from the min. bias trigger. Thus a balance between total dead time and downscale factor must be chosen.

2.3.2 Data storage

The digital signals have to be further processed and permanently stored. This is done by the central DAQ which collects all digital information from the different detector systems and arranges them event-wise and writes them to list mode files (.lmd). The DAQ is a combination of hardware and software relying on the MBS system. Extensive information on the DAQ can be found in [30, 31].

[9]The time at which the full or part of detection system is busy processing the data.

3 Software used for analysis

The large amount of data produced by the setup is treated mainly by three programs. LAND02 is used for unpacking and calibration of the collected data. ROOT is employed for handling unpacked data, both for some calibration procedures and for physics observable extraction. The TRACKER is needed to reconstruct the paths the ions (and other particles like protons and neutrons) took through the setup and is a stage after LAND02, but before physics interpretation. ROOT is a standard tool in high-energy nuclear and particle physics, for more information see Ref. [32]. The other two program packages are developed and used within the LAND/R^{3}B-collaboration and will be briefly introduced in this chapter.

3.1 The LAND02 package

The conversion from raw data to data usable for physics interpretation follows several different levels which are introduced by the calibration and unpacking program package LAND02 developed by H.T. Johansson. The data collected is stored in list-mode-files (.lmd), but analysis usually employs *.root* files. One of the main functions of LAND02 is to read the .lmd files and write the data to *.root* files. Data can be extracted at any of the processed levels (provided calibration parameters exist) and that is also needed during calibration. The program producing these *.root* files is called PAW_NTUPLE. The name is a remnant from the first versions of LAND02 where it wrote PAW-files (see Ref. [33] for information on PAW).

The different levels are indicated in Fig. 3.1 from no treatment (top) to most treatment (bottom). The *raw* level denotes data that is not treated at all (except for the unpacking). At the *tcal* level times are converted to ns and pedestals are subtracted.

At *sync* level the detector is internally synchronized and the energy is in units of MeV for most detectors. *Hit* level data provides positions, times and energies per hit (i.e. per particle hitting a detector) in contrast to previous per channel (or per segment) information. The *dhit* level lies between sync and hit, allowing for an extra step in the calibration needed by some detectors, thus the level of treatment is not uniform over all detectors. At hit level the data is ready for tracking (i.e. reconstructing how the particles traveled through the setup). For the incoming beam this is done inside LAND02 but for the reaction products this is done in the TRACKER.
The second major task of LAND02 is to extract special events suitable to perform calibrations. For some parameters types it even determines the calibration parameters. A few of the most common programs used for calibration are indicated in Fig. 3.1. Calibration routines which are not fully integrated in LAND02 are usually in the form of ROOT-scripts. These scripts use *.root* files with data unpacked at various levels produced by one of the programs of LAND02. For more information see Ref. [23, 30, 31].

3.2 The TRACKER and its usage

The tracker program is independent of LAND02 though it employs data generated with PAW_NTUPLE at track and hit level. It is developed by R. Plag.
The TRACKER calculates the paths of the ions through the setup (on an event-by-event basis) using the Runge-Kutta algorithm. The trajectories are optimized to fit the detector hits provided by LAND02 track and hit level data as good as possible. It is adjustable to the different experiments performed at the LAND/R^{3}B-setup. Its main function is to determine the mass of the outgoing fragments, whose charge has to be supplied by the user[1)]. It is able to apply cuts on any of the measured quantities, e.g. to perform the charge identification or to track only a certain species through the setup. The tracker itself needs to be calibrated, i.e. the positions of the detectors have to be determined to a very high degree of accuracy. The detector positions

[1] The charge is reconstructed based on detector information, Sec. 6.1.1 describes how.

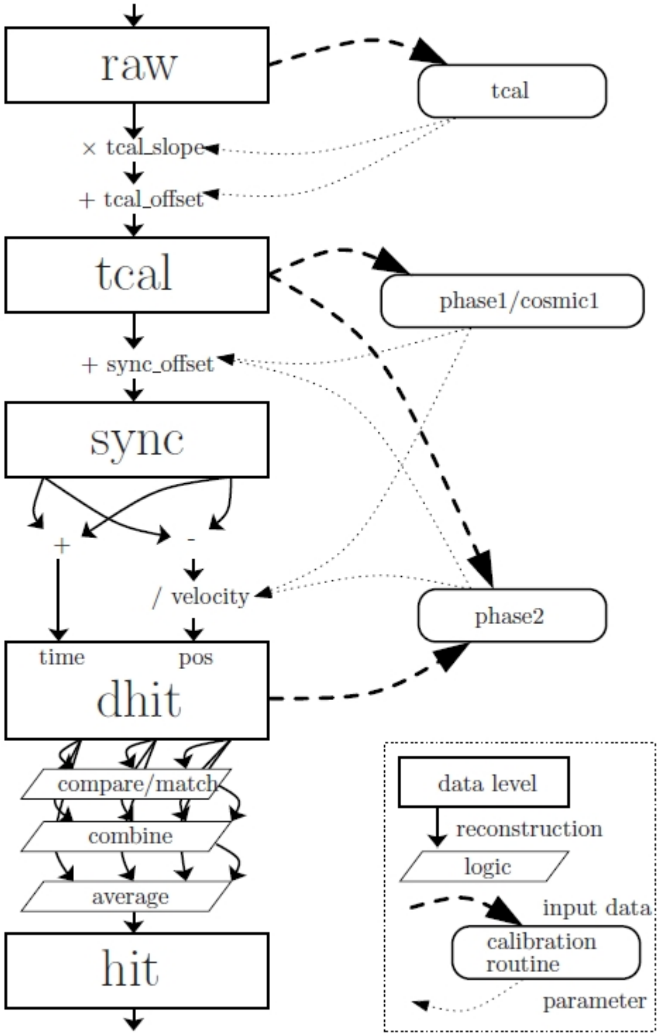

Figure 3.1: Illustration of the work-flow of LAND02. Picture taken from Ref. [31].

determined by laser measurements or photogrammetry are not sufficiently accurate. Only by tracking a known ion[2)] it is possible to fine-tune the detector positions, calibrating the tracker.
In order to determine the mass of an ion with a certain charge, the tracker uses the direction of the ion before the magnet (derived from the SST detectors), the direction of the ion behind the target (derived from GFI x-direction) and TFW (y-direction) detectors), as well as the the charge of the ion and the magnetic field in ALADiN to calculate the track of the ion. That provides the velocity and mass of the ion.
The tracker also calculates the direction of the incoming ion. Since only one half of the first SST was working, the incoming direction cannot be inferred from the two positions in the SSTs before the target[3)]. Therefore the position in the target and the position in the second SST before the target are used. The position in the target is, in turn, derived from backtracking the outgoing fragment back to the middle of the target, defining this point as the interaction point.
Additionally, after the interaction point in the target is determined, the direction of outgoing neutrons is corrected with the position in the target. Likewise, after determination of the velocity (β) of the fragment, the energies detected in the Crystal Ball are Doppler-corrected. In principle, the tracker could also provide a discrimination between photons and heavy particles, but this is not implemented yet, and due to malfunctioning of the box-SST detectors anyhow not possible for the present experiment. Thus the tracker only performs a Doppler-correction to all hits, leaving it to the user to discriminate photons from particles[4)].
More information about the TRACKER can be found in Ref. [34].

[2]By using an empty target measurement, for example.
[3]In principle it can be done, but only for approximately half of the events.
[4]More explicitly, it generates a new quantity and the reconstructed energy deposit is not overwritten.

4 Calibration of the Setup

This Chapter describes the different information provided by each detector and the calibration of each of them. Since a large part of the detectors is based on plastic scintillator paddles these are grouped into one section. All other detectors exhibit special features and their calibrations are therefore described separately. A summary of which detectors were used in this work and whose calibrations were used is shown in Table 4.1 at the end of this Chapter.

4.1 Reconstruction in a paddle-based plastic scintillator detector

Usually plastic scintillator detectors provide energy and time. Due to light attenuation, the light pulse, and thus the PMT current, and consequently the energy detected in that channel is dependent on the distance between point of interaction (hit) and the

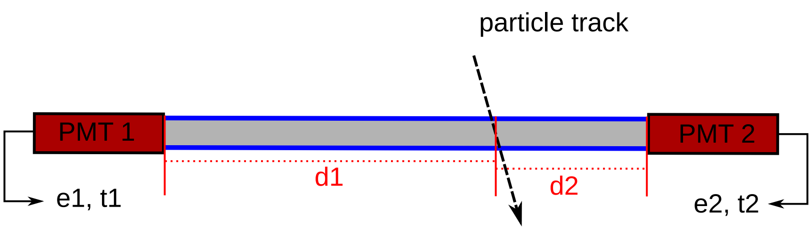

Figure 4.1: Sketch of a particle passing through a scintillator bar with a PMT mounted at each side. The distances d_1 and d_2 can be derived from the energy and the time signals independently (e_1, e_2, t_1, t_2).

PMT. Also the time depends on this distance, as soon as the size of the scintillator becomes significant, i.e. if light travel times inside the scintillator reach the order of magnitude of the achievable time resolution. This has the drawback that one needs to compensate for that, usually using two PMTs at opposite ends of the detector. This also offers the possibility to derive the hit position from the timing and energy measurements. This will be shown in the following for a scintillator bar of length L with PMT read-out at each end. See Fig. 4.1 for nomenclature.
When a particle strikes the scintillator at time T, the two channels will report times:

$$\begin{aligned} t_1 &= T + \frac{d_1}{v} \\ t_2 &= T + \frac{d_2}{v} \end{aligned} \tag{4.1}$$

Where v is the speed of light in the scintillator. This time information can be used to deduce the time T and the place $x(= d_1 - \frac{L}{2})$ at which the paddle was hit:

$$\begin{aligned} T &= \frac{t_1 + t_2}{2} + \frac{L}{2v} \\ x = d_1 - \frac{L}{2} &= v\frac{t_1 - t_2}{2} \end{aligned} \tag{4.2}$$

The terms $\frac{L}{2v}$ and v are detector constants and can be included in the calibration parameters.
Likewise is it possible to deduce the deposited energy E and the location x from the two energy recordings:

$$\begin{aligned} e_1 &= E \cdot e^{-\frac{d_1}{\lambda}} \\ e_2 &= E \cdot e^{-\frac{d_2}{\lambda}} \end{aligned} \tag{4.3}$$

with λ being the attenuation length of the scintillator. A bit of rearranging gives the total energy deposited E and the position x where the paddle was hit:

$$\begin{aligned} E &= e^{\frac{L}{2\lambda}}\sqrt{e_1 e_2} \\ d_1 &= \frac{1}{2}(L+\lambda\ln(\frac{e_2}{e_1})) \end{aligned} \tag{4.4}$$

Again, the terms $\frac{L}{2}$, λ and $e^{\frac{L}{2\lambda}}$ are detector constants which can be included into calibration parameters. This shows how time energy and position of the hit in a scintillator (bar) can be reconstructed. Similar calculations can also be done for scintillator sheets with 4 read-outs at its sides, like the POS detector.
From these formulas one sees that the times and energies provided by the two different PMTs need to be well synchronized. That means, if a hit is exactly in the middle of the paddle, the energy and time read out at each side should be the same. In order to match the information of several paddles in one detector, all paddles need to be synchronized (i.e. their T and E). The methods to achieve this are described in the following section.

4.2 Calibration of paddle-like plastic scintillator detectors

Knowing how the reconstruction works, it is now possible to embark on the calibration of this type of detectors. There are four programs in LAND02 working with the basic calibration of energy and time read out for detectors consisting of one or more scintillator paddles. These detectors are POS, SCI, DTF, TFW and LAND. In order to bring the detectors to the TCAL level, two pieces of information are necessary: the QDC pedestal and the TDC gain (and the so far arbitrary offset). The QDC pedestal is extracted by the CLOCK program. It uses a specifically generated trigger to extract the average QDC value for zero energy deposit and the width of the zero-energy-deposit distribution. It collects all data with the corresponding trigger, the “clock-trigger”, for each channel and fits a Gaussian to it, which yields average energy pedestal and width[1]. The clock-trigger is generated offspill[2] in regular intervals, when no detector triggered. The TDC gain is extracted with a program called TCAL which uses specifically generated tcal- trigger events. The tcal-trigger is generated continuously during the experiment (as the clock-trigger is) and provides both a start and a stop signal. The time interval between start and stop is between 0 ns and 1000 ns long. The interval between 200 ns and 300 ns has a higher rate and in that interval there are 11 time differences with an even higher rate, such that there are eleven peaks on a flat continuous top, on a flat continuous background. The TCAL program filters these signals out and determines the TDC gain via a fit of the recorded time difference and the actual start-stop delay (recorded for each event)[3]. It also produces an offset which is rather meaningless, as the different channels still have to be synchronized.

The time synchronization and the gain-matching are performed simultaneously in one of the two available programs. There are two programs since it is better to use cosmic muons for the synchronization of the neutron detector, instead of physics events as for the other detectors. The difference between the programs is given by the type of events they use for processing, not how the synchronization is done. The program for LAND is called COSMIC1 and uses cosmic muons traversing the detector. Due to the segmentation of the detector it is possible to track the muons passing through it. Events with suitable muon tracks are selected[4]. The program collects time differences between signals from the different PMTs on one paddle, time differences between different PMTs of adjacent paddles, and as well the corresponding energies. The PHASE1 program works in a similar manner, but collects data from physics events. It is important that as much as possible of the detector in question is illuminated by the beam[5].

If the detector consists of more than one paddle with two read-outs each, the programs first synchronize the two channels of each paddle. This is done by determin-

[1] The calibration parameters are called ENERGY_ZERO_NOISE.

[2] Due to the bunched beam, there are times where ions arrive at the cave, called “inspill” and times when no ions arrive at the cave, called “offspill”.

[3] The calibration parameters are called TIME_CALIB.

[4] Traversing the paddles in a predefined way.

[5] Full illumination is usually not possible, but beams impinging onto a target usually have large enough spread (in position).

ing the average time offsets between the two channels and compensating for it[6], and by determining the average ratio of detected energies and correcting it to be unity[7]. Since the ratio of energies and times depends on the hit position in the paddle, this information is retrieved from hits in crossing paddles. To completely align all channels of the detector, the different paddles have to be synchronized, or correspondingly the different channels of one detector if it consists of only one scintillator (the previous step is skipped then). This is still done by COSMIC1 or PHASE1 using data from neighbouring paddles being hit. In the same manner as described above, energy ratios and time offsets are collected for adjacent paddles. These are used as an input to the corresponding sets of equations to compute the needed offsets (time) and gain factors (energy) to generate a completely synchronized detector[8], though only internally.

The synchronization of the setup, i.e. all detectors are synchronized to POS, is different for each detector and will be described for each of them separately[9]. The calibration, except for the final synchronization, is easiest done by scripts from Ref. [35] developed for the collaboration, and they have been used by the author. The parameters and how they are used to calibrate the time and energies can be summarized in the following equations, 1 and 2 indicating the two different channels from one paddle. For the times:

$$\begin{aligned} T_1 &= g_{raw \rightsquigarrow ns} \cdot t_{1,raw} + T_{1,calib} + T_{diff} + T_{sync,det} + T_{sync,setup} \\ T_2 &= g_{raw \rightsquigarrow ns} \cdot t_{2,raw} + T_{2,calib} - T_{diff} + T_{sync,det} + T_{sync,setup} \end{aligned} \tag{4.5}$$

For energies:

$$\begin{aligned} E_1 &= (e_{1,raw} - p_1) \cdot g_{1,raw \rightsquigarrow MeV} \cdot E_{diff} \cdot E_{sync,det} \\ E_2 &= (e_{2,raw} - p_2) \cdot g_{2,raw \rightsquigarrow MeV} \cdot \frac{1}{E_{diff}} \cdot E_{sync,det} \end{aligned} \tag{4.6}$$

[6]This parameter is called TIME_DIFF_OFFSET.
[7]This parameter is called ENERGY_DIFF_GAIN.
[8]These calibration factors are called TIME_SYNC_OFFSET and ENERGY_SYNC_GAIN.
[9]The name of the calibration parameter is however the same and is TIME_SYNC_OFFSET, just applied to the whole detector. If several such parameters are supplied they are additive.

4.2.1 Calibration of POS and SCI

As mentioned earlier, SCI1 did not work, so only POS and SCI2 need to be calibrated. The calibration is performed as described above, though only one synchronization step is necessary, since the detectors consist only of one sheet of plastic scintillator. After each detector is synchronized with itself, the two detectors need to be synchronized in order to provide a physical ToF measurement. This last step is done manually. The exact distance between SCI2 and POS has to be calculated (depends on the flightpath) as well as the expected ToF. This is done for two beam energies and the difference between measured and expected time is calculated and can be corrected for.

4.2.2 Calibration of LAND

The neutron detector LAND needs calibration of both the energy and the time branch. As mentioned earlier, it needs to be synchronized with POS to provide a physical ToF. There are two possible methods. One uses the “gamma-flash” which is created when the ions interact with the target and emitted into forward direction. For that one just needs to calculate the distance for each hit reconstructed in LAND and plot the thus corrected ToF. The gamma peak is visible as a sharp spike in the beginning of the spectrum and the offset has to be adjusted such that its mean value corresponds to particles traveling at light-speed. The second method requires that the incoming beam detectors and the detectors in the fragment arm are already calibrated. If that is the case, one can track a reaction in which a neutron is emitted (from e.g. a neutron unbound state which is created in that reaction) and determine the time offset correction from the fact that the average β of the fragment should coincide with the average β of the neutron.

4.2.3 Calibration of the TFW

The TFW needs a calibration as described above. For the final synchronization to yield a physical ToF between TFW and POS, it is easiest to use the TRACKER (which requires that the incoming beam detectors are calibrated as well as the positions of all fragment arm detectors). For an unreacted beam the incoming and outgoing β should be the same except for energy loss according to the Bethe-Bloch formula. Since the TRACKER accounts for that, and can even calculate the difference between measured and expected times assuming the βs are identical, this is the easiest way to calibrate the TFW time offset.

4.2.4 Calibration of the DTF

The DTF calibration is done exactly as described above. The DTF calibration was only implemented into part of the aforementioned scripts from Ref. [35] handling with TCAL and CLOCK, thus it had to be implemented into the synchronization phase, which was possible with minor changes. Due to the structure of the detector with only three crossing paddles, the calibration might not be reliable though. The DTF has not been used further in this work. The final synchronization with POS has not been performed, but can be done using the proton tracking capabilities of the TRACKER for example.

4.3 Calibration of the PSP

The PSP provides only energy signals. One signal comes from the cathode, and one from each corner. Out of the four energy signals from the corners a position can also be derived.

First the cathode channel is calibrated using different beam energies and/or different beam species. The positions of the means for the different peaks can be fitted to the Bethe-Bloch formula in order to obtain a charge calibration. The ratios of the energy deposits in the left and right or up and down corners, give information about the position in x- and y-direction the detector was hit at. In order to calibrate the position, usually a pixel-mask is inserted in front of the PSP and the position of the pixels can be correlated with the energy fractions. Unfortunately there was not enough data collected with the pixel-mask and therefore it is not possible to calibrate the PSP with that method. Fortunately it is possible to extrapolate the particle tracks back from the SSTs onto the PSP and using that position perform a calibration. This work is still in progress by S. Lindberg.

4.4 Calibration of the SST detectors

The information provided by the SST detectors is the deposited energy while the hit position is conveyed by which strip(s) detected the particle. The energy calibration needs, as in other detectors, a pedestal subtraction, which can be extracted by the CLOCK program. All further calibration steps are not incorporated into LAND02 yet. For the present experiment Matthias Holl has developed a set of routines which perform the calibrations described. The routines are available at [23]. The strips record a different energy depending on where they are hit, even more pronounced in the S-side capacitively coupled strips. Thus corrections depending on where the strip is hit is necessary. The internal coordinate across one strip is called η.
The routine extracts the integral of the normalized histogram of η and fits a 9^{th} degree polynomial to it. This distribution is then given to LAND02, though as LAND02 cannot read calibration functions yet, as an array of 100 points which LAND02 transforms into a function again. This function is used to correctly infer the position in the strip. This function is collected detector-side-wise, not strip-wise[10)].
After this is done, the energies of the strips need to be gain-matched. This should only be done after the position correction, since this correction depends on the position. The routine developed for this divides each strip into 3 bins and fits a Gaussian to the energy, the energy in each strip is then normalized to the average of all strips in one detector and the normalization factor is stored as synchronization factor[11)].
Finally the energy deposited inside the strip needs to be corrected depending on η. This is done by deriving the normalization factor (depending on η) such that the energy detected in the strip is independent of the position[12)].

[10)] The calibration parameters are called SST_POS_CORRECTION.
[11)] This calibration cannot be applied by LAND02 yet - so there is no name yet either.
[12)] This calibration can be applied by LAND02 again and the parameter is called SST_GAIN_CORRECTION

4.5 Calibration of the Crystal Ball detector

Energy calibration for the low-energy branch

Typically the low-energy branch calibration is done using data collected with a γ-source. The peaks in the gamma spectrum for each crystal are fitted with a Gaussian on a linear background. The (γ-)peak positions and their corresponding energies from all gamma peaks are then linearly interpolated yielding gain and offset.
This method has two main drawbacks, one is that gamma energies of standard sources can reach only up to 4 MeV, but gammas emitted by the fragments can have energies up to 15 MeV due to Doppler boosting. Small errors in the calibration at low energies develop therefore a large leverage and can be significant at higher energies. The second problem, which turns out to be quite severe, is that it is difficult to ensure a regular check of the calibration[13)]. Calibration source runs require beam breaks, in which the cave is accessible such that a person can go in, open the XB and place a source. Since this is quite an effort, and expensive and valuable beam time usually gets lost, people tend to forget the necessity of regular calibration runs. Without regular calibration runs though, it is not possible to be sure of the validity of the calibration, rendering data useless or only usable with high uncertainties. Additionally the XB gain has been found to be unstable. More detail about that and a solution to this problem is described in Section 5.2.

Energy calibration for the high-energy branch

While the use of gamma sources for the calibration of the low-energy branch is critical, it is not possible to use them for the high-energy branches. Instead, cosmic muons are used to perform the calibration of the 64 high-energy branches. Cosmic muons are usually minimum ionizing and thus deposit a constant energy per unit length. Therefore the path length they travel inside a crystal determines how much energy the muons deposit in it. Selecting certain paths, by muon tracking through the detector, thus allows choosing a certain energy deposit. The routine GAMMA2

[13)] In principle one can only be sure of the validity of the calibration during the time the data used for it was collected. So in order to trust the calibration one needs to show that a detector is not drifting (i.e. the gain stays constant with time). The opposite was unfortunately observed for this detector.

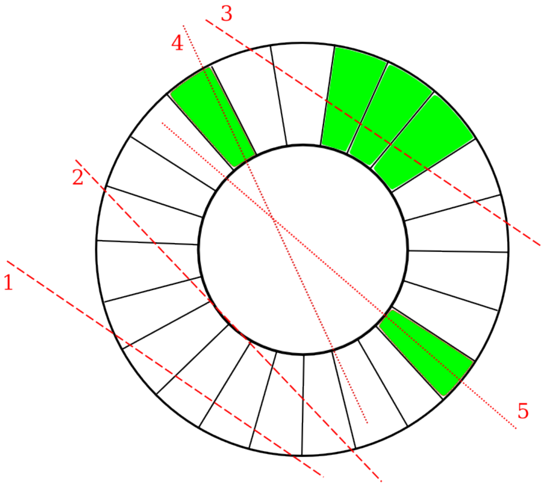

Figure 4.2: Schematic sketch of muons traversing the XB. Paths 1, 2, and 3 indicate potential “grazing” muon events, whereas 4 and 5 indicate opposite muon events. Energy information is stored for crystals marked in green. Path 1 and 2 are both not taken for data collections as path 1 is too short and path 2 is too long for a well defined path-length.

performs the tracking and collects the events where muons traveled such defined paths inside a crystal. There are two classes of paths which are used, as indicated in Fig. 4.2 and they are called opposite and grazing events. The opposite events are such that a muon traverses the length of a crystal fully, i.e. traveling about 20 cm through the crystal. The grazing events are events where a muon traveled through a chain of neighbouring crystals, i.e. grazing through the shell. The length of this chain has to be between 5 and 8 crystals in order to ensure that the muon traveled along a well-defined path through the central crystals of the chain, for which the energy deposit is used for calibration. A more detailed description of the identification algorithm and the different events can be found in [36].

According to simple simulations [37], the opposite and grazing events deposit around 90 MeV and 45 MeV in the crystal of interest respectively. This is not exactly in the middle of the range which goes up to around 300 MeV, but the situation is significantly better than in the low-energy branch.

A different problem is that it has been shown that muon energy deposit and proton energy deposit do not scale 1:1 [38]. This issue is not completely solved, so the energy calibration of the high-energy branch cannot be regarded as final yet. Generally the energy calibration has been done with the full statistics of offspill events of one experiment. This was performed as a first approximation, but since a large drift was found in the low-energy branch, also the high-energy branch has been calibrated on a day-to-day basis. The development of this procedure is described in Section 5.2.

Time calibration

The time calibration for the XB is quite straightforward. The TDC gain is known and is not something which has to be derived, thus there is no calibration needed to transfer the timing information into ns. Then, as usual, the different parts of the detector, i.e. the different crystals have to be synchronized. There exists a routine in LAND02 inside the GAMMA2 routine which is dedicated to the timing synchronization of Crystal Ball. It works on the basis that the low-energy branch has been calibrated. The routine employs source data[14)] taken with a gamma source which has at least a two-gamma cascade. By identifying the crystals which detected the gammas (energy windows), the routine collects time differences between all crystal pairs. If more than two crystals detected the requested energies the event is discarded. After collecting sufficient statistics the time difference spectra are fitted in order to derive the mean time difference for each crystal pair with sufficient statistics. These mean time differences are then used to compute the different offsets (in time) of the crystals compared to a XB local zero. The XB is thus synchronized internally but not with the setup, but that is also not necessary for its purpose. For further details see Ref. [36].

4.6 Calibration of the GFI

Though the GFI are only supposed to give a position information, this information is conveyed by the energy detected in the fibers. The timing PMT signal is used for

[14] Currently it is equipped for ^{22}Na, ^{60}Co and ^{88}Y, but new sources can be added easily.

trigger purposes and does not need to be calibrated. In order to calibrate the energies of the different pixels in the PSPM (position sensitive photo multiplier), the pedestals need to be determined, and this can be done using CLOCK as for most detectors. After that, the different channels need to be gain-matched, since the PSPM usually has a higher gain in the centre compared with the sides. This is done by a modified PHASE1 program, PHASE1_GFI, which is adjusted to the fact that there are no crossed paddles, but fibers. After these two things are accomplished it is possible to match "pixels", i.e. fiber endings on the PMT to the respective fiber. This is not done by LAND02 but by a set of scripts available to the collaboration written by K. Mahata. For this, preferably a data file in which the full GFI is illuminated should be used. The routine generates a 2D histogram in the internal coordinates (u,v) of the PMT and counts the amounts of hits in each bin above a user specified energy threshold. From that histogram the routine tries to locate clusters. Each cluster corresponds to one fiber ending. The cluster centers are found by a Gaussian fit, and these are mapped to the fibers according to the scheme displayed in Fig. 4.3. The user should inspect the mapping visually if it fits the intended mapping or whether the routine made a mistake. If so, one needs to adjust either the threshold for data taken into account or the presumed cluster radii. An example of how the plots for visual inspection look like is shown in Fig. 4.4, displaying the actual mapping in the S393 experiment used in the present work.

4.7 Calibration of the PDC

The information provided from the PDC is the wire number, the time when the pulse went over threshold and the time when the pulse went below threshold, for each wire over threshold. The information which should be extracted is the position in x and y direction in each detector. Since the gain of the timing branch is provided by the modules and written in the data files, this calibration factor does not need to be extracted. Before the drift times can be converted into positions, the detectors need to be synchronized with POS[15)]. In this case synchronizing means that the time

[15]This uses the known parameter TIME_SYNC_OFFSET.

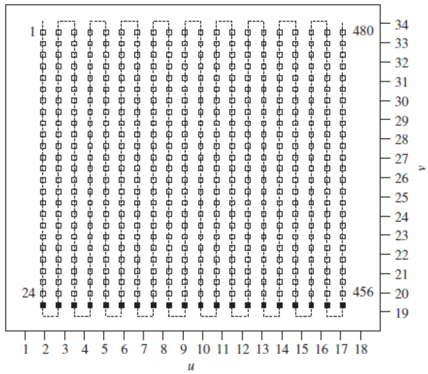

Figure 4.3: Illustration of how the mapping between cluster and fiber positions is done. Taken from Ref. [28].

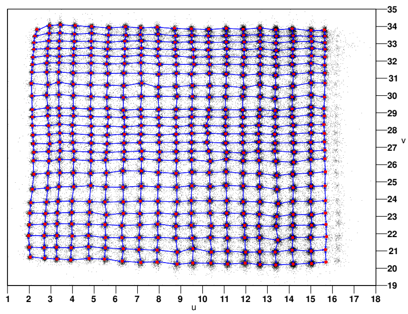

Figure 4.4: Plot of the actual mapping. Black dots are data points, red circles the identified cluster centers and the lines show the neighbour connections.

spectrum should be shifted to start at zero when the POS time is subtracted. To extract the position, so-called xt-curves are necessary. They are created under the assumption that each path at a certain distance from the wire through a cell is equally likely, which is true for the central cells[16)]. Thus the start-times should be distributed equally as a rectangle in a histogram. The xt-curve is calculated such that the start-times match the rectangle. This is done in the unpacking program PAW_NTUPLE if the corresponding flag is set, and requires no further user intervention. The xt-curve is given as a list of time and position pairs[17)]. A more detailed description can be found in Ref. [23].

[16] In x-direction the central cell is defined by the beam centre.
[17] This calibration parameter is called PDC_XTC_POINT.

Detector	used in this work	calibrated by
SCI1	no	-
SCI2	yes	M. Heine
POS	yes	M. Heine
PSP	yes	M. Heine
SST	yes	M. Holl
XB	yes	R. Thies
LAND	yes	C. Caesar, R.Thies
GFI	yes	R. Thies
TFW	yes	R. Thies
PDC	no	A. Najafi
DTF	no	R. Thies

Table 4.1: Overview of detectors used in this work. The third column indicates who of the R^3B collaborators (PhD students) performed the calibration used. The internal calibration of LAND by C. Caesar was used, but the synchronization with the setup was done by R. Thies.

5 Developments

In this Chapter own developments, performed within this thesis work, in order to improve data analysis of LAND/R^{3}B experiments or crucial to the analysis of S393 are described. The first section outlines the developments in order to recover parts of the beam which were misidentified due to a malfunctioning detector. In the following section the means which were developed in order to perform a continuous calibration of Crystal Ball are set forth. A delineation of the implementation of an addback routine for Crystal Ball into LAND02 and its functioning is given in Sec. 5.3. This is accompanied by a short digression on how the addback affects reconstructed energies. The development and implementation of a cosmic muon generator into the GGLAND framework is described in the last section of this chapter. It is used to improve the high-energy branch calibration of the Crystal Ball.

5.1 Incoming beam

This section describes the problem which occurred due to malfunctioning of the beam detectors at FRS during the S393 experiment, and the solution that was developed. The two detectors at S2 and S8 are used for ToF measurements together with the POS detector at the experimental setup. The detector at S2 was not working at all, and thus not usable during the experiment. Additionally the detector SCI2 at S8 developed an unusual behavior in the course of the experiment, first seen in the identification plots. Identification plots show the reconstructed charge (from energy deposits) versus the reconstructed mass-over-charge ratio (from separator settings and ToF) for the incoming ions. Fig. 5.1 shows expected (5.1b) and recorded (5.1a) identification plots. Looking at the time spectra of the two S8 PMTs, one can indeed

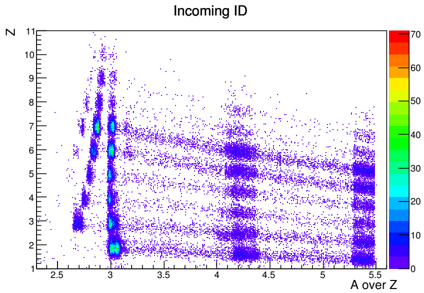

(a) Incoming ID due to the broken detector SCI2 at S8.

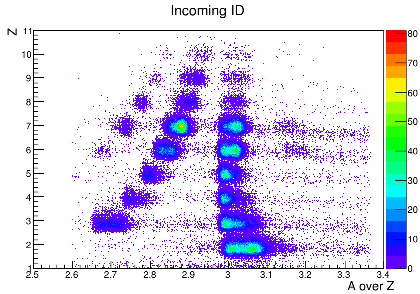

(b) Expected incoming ID.

Figure 5.1: Identification plots: the originally detected one, due to the malfunctioning detector at S8 (left), and the expected (and later recovered) identification plots (right) are shown here. Data collected with the Physics triggers are used.

identify unexpected behavior, namely uncorrelated times. As the ToF between S8 and the setup, which triggers the Master Start, is long, one expects a good correlation which is smeared when plotting, but not destroyed by jitter in the MS. Different flight paths and the different possible positions the detector at S8 can be hit at also contribute to the smearing. The actually measured times are shown in Fig. 5.2a, where more than the expected structures can be seen.

From that plot it is obvious that sometimes one time signal is uncorrelated to the other and the expected time difference. This becomes more explicit in Fig. 5.2b. The problem of a channel (or both) missing the correct signal was caused by the settings of the CFDs used. The output of the CFD was too long, such that a signal from an ion close by in time (a few hundred ns) is masked and not seen by the CFD. Light particles might cause only one of the CFDs to trigger, explaining the cases with one incorrect time.[1)]

The suggested solution sounds simple, identification of the PMT which did not receive a signal from the correct ion, and usage of only the other PMT, loosing a little bit of accuracy. The loss of accuracy is due to the fact that the distance from the

[1]The SCI2 detector is located directly behind the last separating magnet and thus might still be hit by a significant amount of ions, both light and heavy, not arriving at the setup.

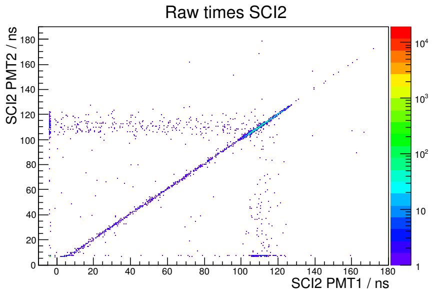

(a) Times from the S8 detector (SCI2).

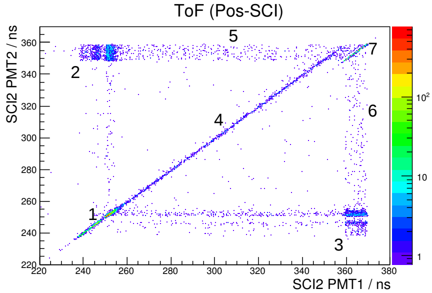

(b) ToF between POS and S8.

Figure 5.2: Correlation of the times provided by the two PMTs of SCI2. Left shows the times of the two PMTs vs. Master Start, and right shows the ToF deduced from each PMT with the help of POS. Data collected with the Physics triggers is shown. *Region 1* consists of good events; events from *region 2 and 3* can be recovered. For details see text.

PMT at which the ion hit the scintillator cannot be corrected for with only one PMT, but since the detector is only 22 cm wide, in comparison to the about 55 m long flightpath, this does not cause a significant uncertainty. This method does of course require that the two PMTs are correctly synchronized.

The task is thus to identify the events in which one PMT at S8 did not provide a signal. This should be easily identified even in the non-physical time spectra SCI2 versus MS, as seen in Fig. 5.2a. Unfortunately, this is not possible for the S393 data because the MS comes after the accepted triggers, and one of the detectors required for the main reaction triggers (XB) came late. The result is a jump of the MS in time depending on the detector which triggered. Therefore, the physical quantity of ToF, i.e. the difference of SCI2 time and POS time (seen in Fig. 5.2b) is used in order to identify the events in which one PMT missed the signal.

This does have the advantage of being independent of the jittering MS, and actually recovering a larger amount of events. The only drawback is that one actually cuts in a physical quantity in order to recover it, which is not a good practice. As data from only one ToF detector at the FRS is available, there is no other choice.

In order to be able to recover the times, it is essential to understand first what the different parts of the spectrum represent. As the ToF is used directly, the different features of it are explained in the following. *Region 1* in Fig. 5.2b consists of events where both PMTs provided a good and correlated time. *Region 2 and 3* represent events for which one PMT provided a signal in the expected time window, while the other provided nothing (most statistics in that region) or an arbitrary time. *Region 4* consists of correlated time signals from both PMTs, but not in the time window of a signal in POS in which ions reaching the set-up are. These events are random coincides and pile-up effects. *Region 5 and 6* represent events in which one PMT did not give a time signal and the other provided a timing outside the expected window for ions reaching the set-up. *Region 7* might look surprisingly correlated, but consists essentially of events in which both PMTs at S8 provided no signal corresponding to the one detected at POS.

In principle, there are several ways to fix the problem of misidentified events. One could for example simply require that both PMTs deliver a proper timing signal. This would, however, reduce statistics significantly. The goal is to recover as many events as possible. Events that can be recovered are located in *region 2 and 3*. If there had been a second working ToF detector at the FRS, one would also have been able to recover events (not necessarily all) from *region 7*[2)].

The identification and recovery of events has been implemented in the unpacking routine of the program-package LAND02 which is used for calibrations and unpacking of data collected at the LAND/R^{3}B setup. The principles of this program package are illustrated in [31] and a more hands-on users guide can be found at [23]. Important to note is that the unpacking routine goes through unpacking stages from RAW to HIT as illustrated in Sec. 3.1, for all detectors. Information are usually not communicated between routines for different detectors. This, though, is needed for this recovery as information from the POS detector on DHIT level is required to perform the recovery of SCI2 times (to the DHIT level). In order to recover the events from regions two and three, one identifies these regions by conditions on the times POS - SCI2 and assumes instead of an average of both PMT times, as done for *region 1*, the time from the PMT which delivered a signal correlated with the POS signal as the

[2]These events are there due to the efficiency not being 100%. Since SCI1 would also not have 100% efficiency, not all events from *region 7* could have been recovered.

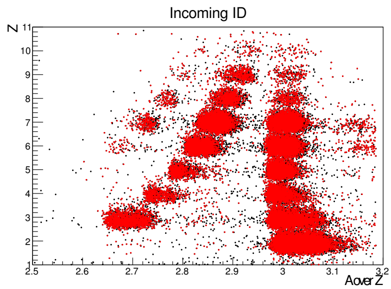

(a) Events reconstructed from region one (c.f Fig. 5.1b).

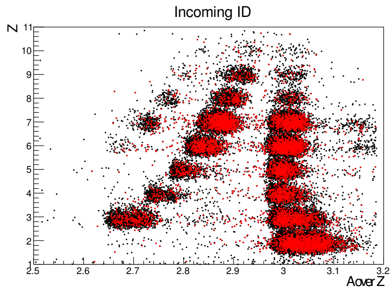

(b) Events reconstructed from region two (c.f Fig. 5.1b).

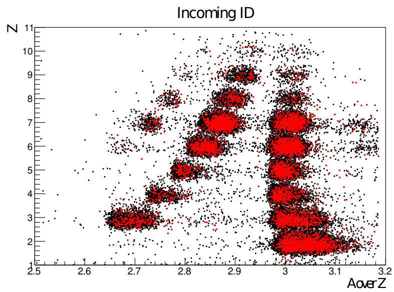

(c) Events reconstructed from region three (c.f Fig. 5.1b).

Figure 5.3: Identification plots. Black indicates the total events recovered while red indicates the events recovered for the selection mentioned in the captions. Only a fraction of the total statistics is shown.

time information from SCI2. This method does of course still introduce a little bias, as the time the light has to travel in the small scintillator is not accounted for. For this method to work, the synchronization of the PMTs from SCI2 is crucial, which can be achieved e.g. by using only data from *region 1* during the alignment. If the PMTs are not perfectly synchronized, an offset is introduced when recovering the ToF from the information of only one PMT.
The results from this method for recovery of events are good, as indicated in Fig. 5.3. What can also be seen from Fig. 5.3a is that the major part of the statistics stems from

events in which both PMTs from SCI2 delivered a signal.

5.2 Time-wise continuous calibration of Crystal Ball

As described in Sec. 4.5 the Crystal Ball needs a time and an energy calibration. Previously, calibration of the Crystal Ball was performed using source-runs from before, after and, if available, during breaks in the experiment. This implies that one can be sure about the validity of the calibration only during the times source-runs were taken, which means intrinsically that no physics data is collected during times of a reliable calibration. In the present section the development of a routine that uses off-spill data in order to perform the energy calibration is presented. This means that the detector behavior can now be monitored during the experiment (at least for the energy branches) and reduces the need for source-runs in the middle of an experiment. The timing calibration as with its present method cannot be performed without a source of coincident gamma-rays, and is therefore not possible to perform with off-spill data[3)].

The incentive to try monitoring the behavior of the energy branch of the Crystal Ball originates from the discovery of a jump in gain for several crystals during a source run in the S393 experiment. The jump in gain is illustrated in Fig. 5.4.

After that discovery, the peak at 1.46 MeV, stemming from the decay of ^{40}K present in the background, was used to monitor the detector gain throughout the experiment. Combining statistics collected off-spill during three days of the experiment were necessary to allow for a reliable peak-finding and -fitting routine. Additional peaks in the off-spill-spectra were found at 511 keV and at 2.6 MeV, the latter attributed to ^{208}Tl decay and the former stemming from β^+ annihilation not being attributable to any specific decay. An example of the energy spectra is shown in Fig. 5.5. The source of the 511 keV gamma rays was not found to be in the center of the Crystal Ball, thus

[3] Adjustments to make it compatible with beam or muon data are probably possible. This has not been done yet, as the timing is expected to be stable.

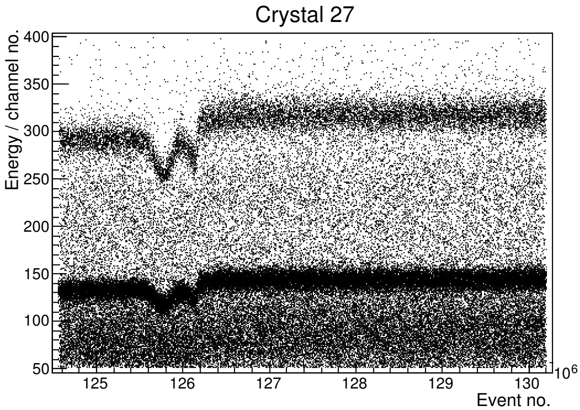

Figure 5.4: Plot of energy versus event number in crystal 27 of the Crystal Ball, illustrating the changes during one calibration run taken with ^{22}Na. Not all crystals had such a strong variation and change in gain.

an activated target holder and similar can be excluded as a source. Instead, the intensity distribution suggests that the 511 keV gamma rays travel in roughly the same direction as the incoming ions. Contrasting to the 511 keV peak being detectable in all crystals, the peak at 2.6 MeV is only well distinguishable in certain crystals.

Since the statistics of three days is needed, the monitoring is not sensitive to sudden jumps other than an increase of the widths of the peaks. In order to increase the sensitivity to variations in gain (and offset) statistics from three days is used as a “moving average” to determine the peak positions (gain/offset) for the central of the three days only, – thus one arrives at day-to-day peak positions but these do not originate from completely independent datasets.

The monitoring, displayed in Fig. 5.6 for certain crystals, showed that a significant amount (about 35 crystals) shows a drift larger than 7 % during the experiment, which is comparable to the broadening due to angular uncertainty when correcting for the Doppler effect. A larger number of crystals have a drift smaller than 7 %, while a few show no significant drift at all. The drift did not show a correlation with the magnetic field strength of ALADiN, as illustrated in Fig. 5.7, nor with the position of the crystal (θ-angle to the z-axis), as shown in Fig. 5.8, and not with the MSCF

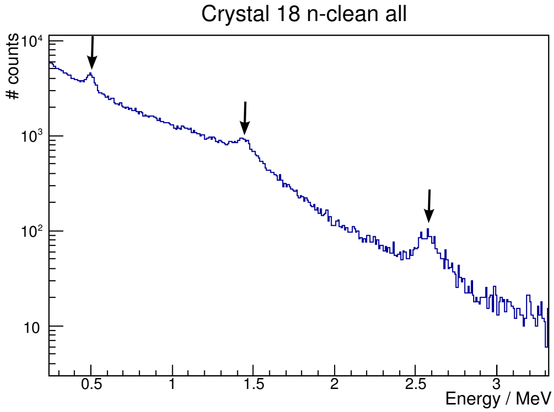

Figure 5.5: Histogram of the energy detected in crystal 18, requiring zero energy deposited in its surrounding crystals, thus improving peak-to-Compton ratio. Peaks are emphasized by the arrows. Statistics from three days is used.

module[4)] the channel was amplified in, as illustrated in Fig. 5.9. The monitoring is performed using the calibration obtained from source runs as described previously (in Sec. 4.5).

When using the previously (insufficiently) calibrated data to calculate new calibration parameters, one introduces significant errors (since the errors of the first calibration propagate). Thus, in order to use the data for calibration, it is sensible to perform peak finding and fitting in the raw data. The scripts for peak finding and fitting were therefore modified once more, in order to be able to do this. They still need a preliminary calibration as input parameter in order to incept proper windows for peak finding and a first preliminary fit. That this is necessary at all is due to the very low signal/noise ratio in particular for the ^{40}K peak (the ^{208}Tl was not used for calibration). Additionally to the day-by-day splitting, the data was split at the time of the jump observed in the calibration run. Data from before and after this jump were not mixed. Thus from day 10 on all days are shifted by one, as day 9 was divided

[4]MSCF stands for Mesytech Spectroscopy amplifier with Constant Fractions, thus amplifies the signal and generates trigger. The same channels which go into one MSCF are also converted in the same ADC.

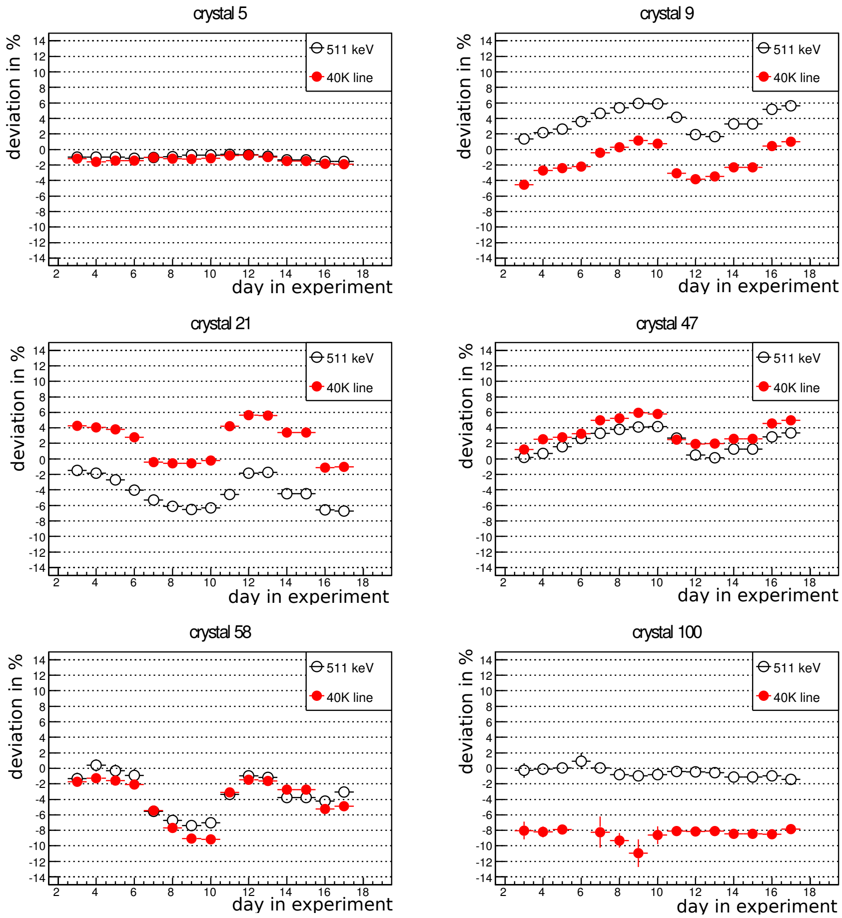

Figure 5.6: Plots showing the deviation from the expected peak positions with the previous calibration in percent. Errors provided by the fit routines are shown, but are mostly smaller than the symbol size. The crystals are chosen in order to demonstrate a spectrum of the different kinds of behavior.

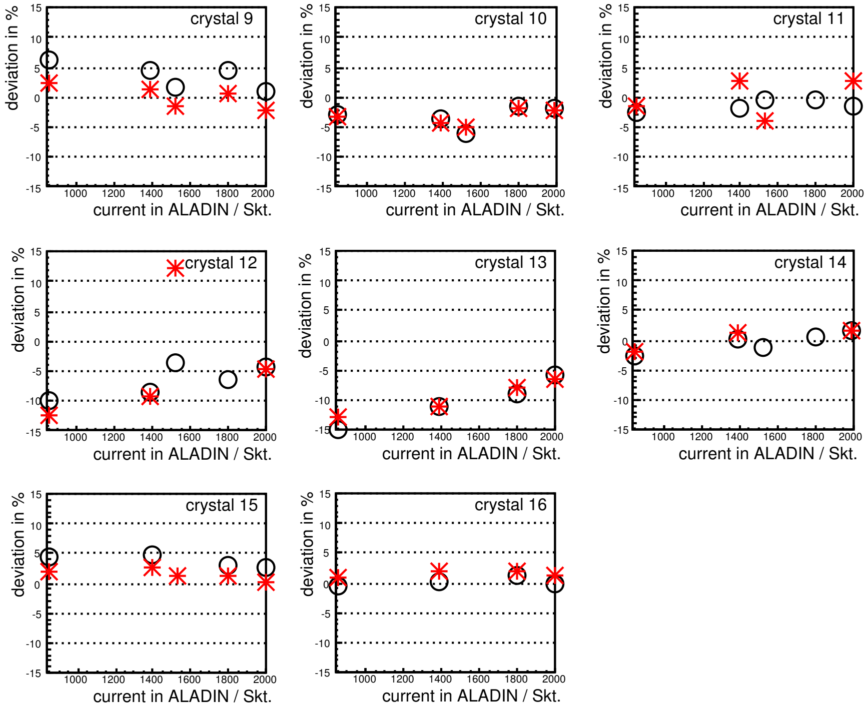

Figure 5.7: Plots showing the deviation of the peak positions from the expected position in percent. Here, the spectra were collected not on a day-by-day basis, but depending on the ALADiN current. Black circles indicate data from 511 keV peaks and red stars indicate data obtained from the potassium line. Symbols are larger than the error bars. No trend is observable. The peaks were broadened (due to the lacking correlation) to the extent that the fitting routine failed for a significant number of crystals, providing strong evidence that there is no dependency on the magnetic field.

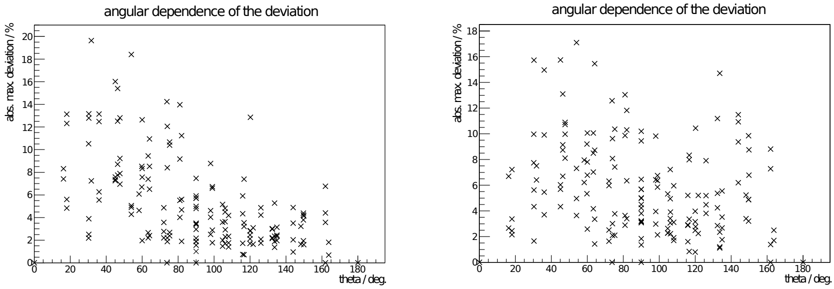

Figure 5.8: Plots displaying the maximum deviation from the expected peak position in percent for each crystal as function of its azimuthal angle. The left plot shows data extracted from the 511 keV peak, and the right one shows data obtained from the potassium line. No clear trend is observable. Errors are smaller than the symbol size.

into two parts. The calibration was tested by fitting the calibrated spectra with statistics from one day[5)] and an improved, satisfactory outcome was achieved with the continuous calibration. Fig. 5.10 shows examples of the different types of improved calibration, illustrating the following classifications. In total 39 % of the crystals are at most 2% off the ideal calibration (e.g. crystal 104) and 37% are off by less than 4% of the perfect calibration (e.g. crystal 137), whereas only 7% of the crystals did not show an improved calibration (e.g. crystal 57). For 3% only one or two datapoints were outside 4% (e.g. crystal 4) and for 14% of the crystals the statistics was insufficient with only one day of statistics (e.g. crystals 43 and 53), such that a significant amount of data points are missing. Generally, the fitting with only one day of calibration needs more manual intervention, as the statistics is is often not good enough. This can also be seen by the errors provided by the fitting routine, which now are significantly larger than in the case of three days of statistics (see Fig. 5.10), supporting the choice of three days of statistics to perform the calibration.

The success of the low-energy branch calibration inspired the same time-sliced cal-

[5] This is not always possible and statistical errors are large. Also good initial values for the fit-parameters used by the fit-routine is needed.

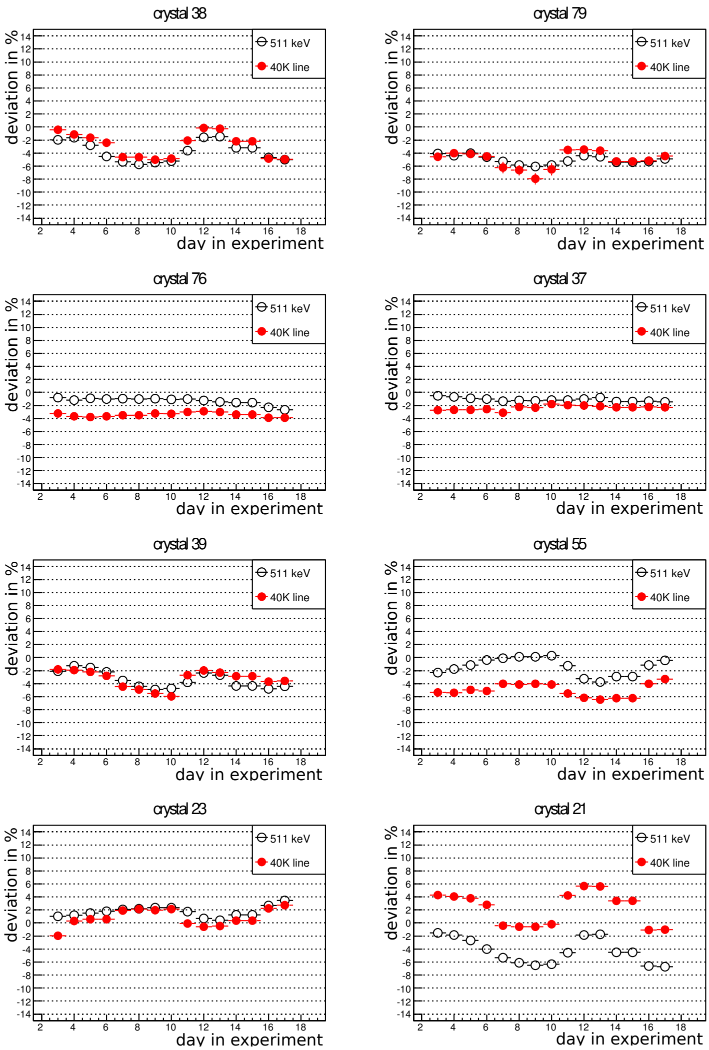

Figure 5.9: Plots presenting the deviation of the peak positions from the expected position in percent. The energy read-out of all displayed crystals is treated by the same MSCF module (not all channels are shown). Errors provided by the fit routines are shown, but often smaller than the symbol size. No general trend is observable excluding the module as a source for the drift.

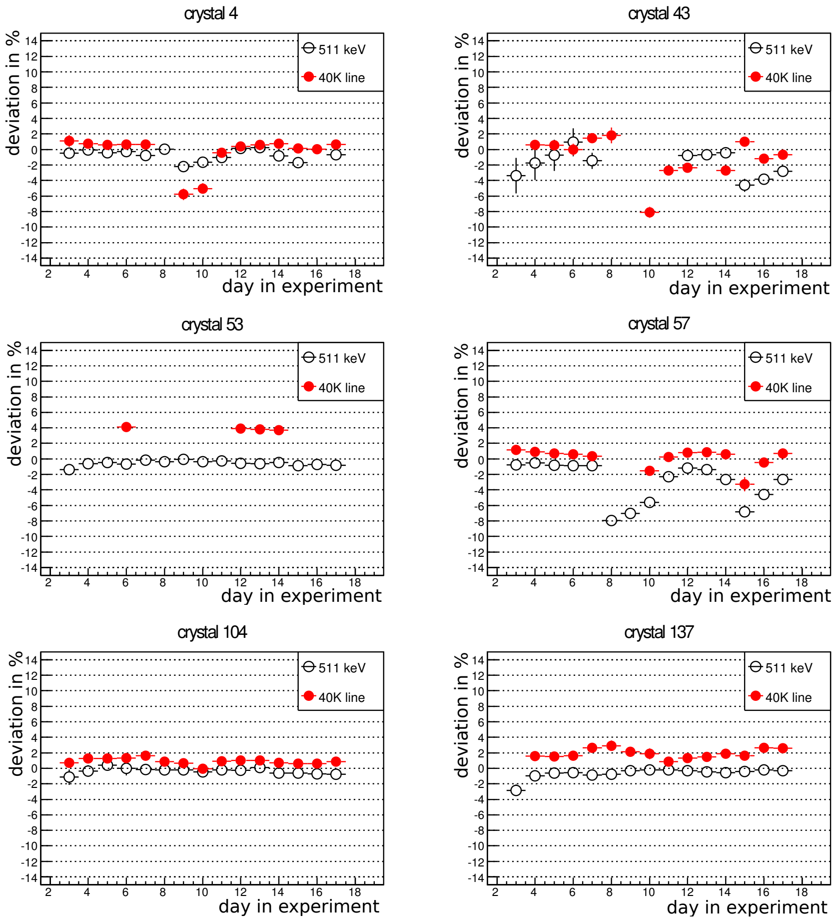

Figure 5.10: Plots showing the peak positions after the continuous calibration. Peak positions are extracted with the statistics of one day. Error bars are the errors provided by the minimization routine (MINOS [39]). Crystals are chosen to give an overview of the different types. For details see text.

ibration for the high-energy read-out branch, which previously had been calibrated using the full off-spill statistics of the experiment. Checking for consistency, one discovers that for most of the crystals the gain of low and high-energy branch vary consistently, as shown in Fig. 5.11, indicating that variations are in fact a PMT-effect. The high-energy branch was thus calibrated continuously with the same method as described above using the two tagged muon tracks. This leads to an improvement of the calibration as one can see by comparing Fig. 5.11 and Fig. 5.12. Here, a lower fraction achieves almost perfect calibration (max. 2% off), 29%, but there are only 5% not-improved calibrations and 10% where it is not possible to fit (fit does not converge / gives very large error bars). Of all crystals with high-energy read-out, 36% can be calibrated to be within 4% off and 21% are fine but have one or two data points which are outliers. These can probably be explained by a failed fit in the control routine. Anyhow one has to note that the most forward crystals are problematic in this approach, as they have very little statistics for opposites (due to few horizontal muons) which is further worsened by the fact that one neighbour is missing, leading to a less effective veto.

Summarizing, it is possible and useful to perform a continuous calibration of the Crystal Ball energy branches. What could be done to improve the scripts is to rewrite them to collect a certain amount of statistics and determine intervals from that instead of fixed times and thus varying statistics. This would require a script controlling the unpacking routine in the best case, while the present scripts could, with adjustments, be used for the rest of the processing. Otherwise the routine can probably not be improved further without a large effort. The 2% uncertainty corresponds to the bin-width of the histograms used and thus one would need more data in order to improve this. That in turn would lead to the need of source runs and thus usually much less frequent data points, resulting, once more, in a larger uncertainty.

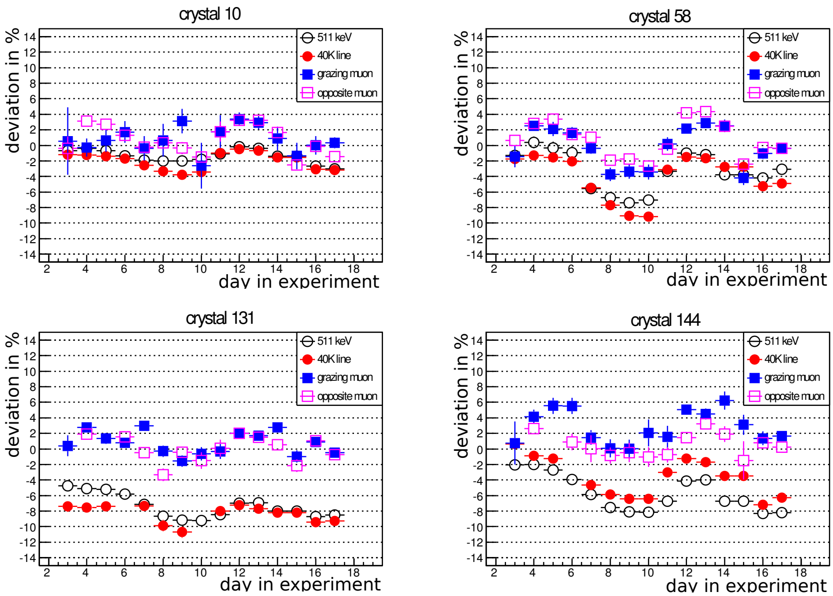

Figure 5.11: Three examples of congruent behavior in the low-energy branch and high-energy branch. Error bars provided by the fit routine. The absolute offset does not match between high and low-energy branches, as expected, but the changes are correlated (though not exactly in absolute scale). Note that day 14 and 15 have the same data for the low-energy branch, as this is the day which was splitted later for calibration, but not when monitoring as for the high-energy branch.

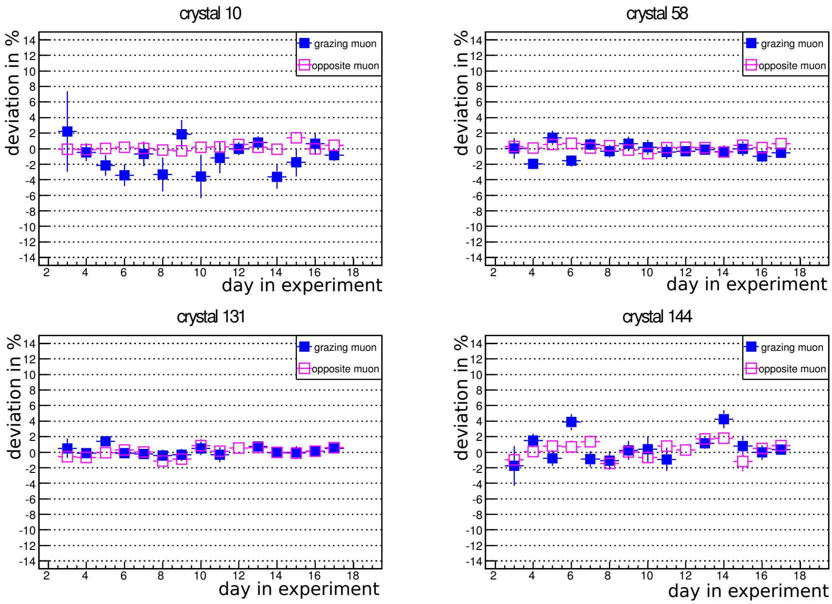

Figure 5.12: The three examples from Fig. 5.11 after the continuous calibration. Errors are larger since now only the statistics of one day is used. For details see text.

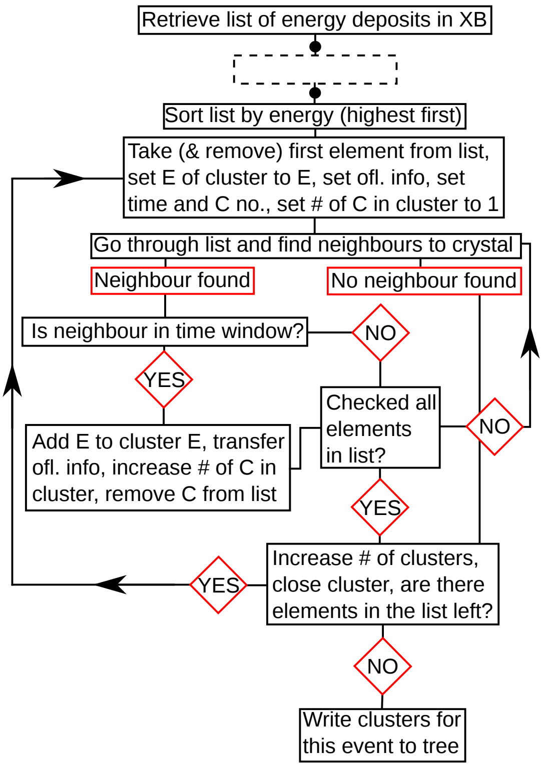

Figure 5.13: Flowchart illustrating the addback routine implemented into the LAND02 framework. The function of the empty box is illustrated in Fig. 5.14.

5.3 Addback-routine for XB

At the energies the experiment is performed at, γ-photons and protons which are supposed to be detected in XB have a significant probability to scatter inside the detector and to deposit their energy in several segments (crystals). As the detector is supposed to be a calorimeter, but usually detects several particles in one event, and additionally is used for discrimination between photons and massive particles, it is important to recover the full deposited energy per particle using addback.

There have been numerous discussions within the R^3B collaboration about how the

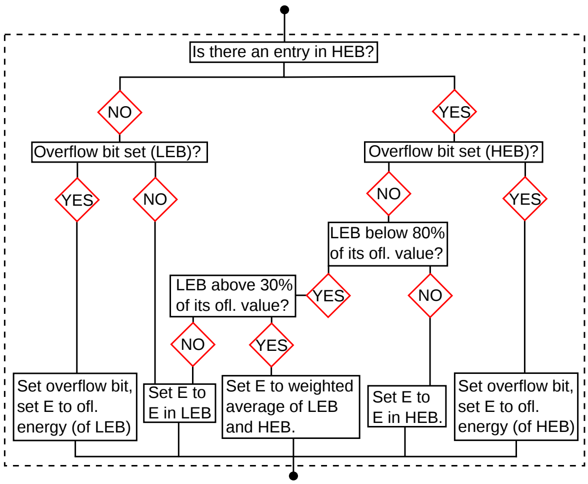

Figure 5.14: Flowchart illustrating the retrieval of energy and overflow information for each crystal. This is done at the very beginning of the addback-routine as illustrated in Fig. 5.13. The abbreviations HEB and LEB denote the High-Energy-Branch and the Low-Energy-Branch of a crystal, respectively.

add-back routine of the XB should look like, at which stage it should be performed, and what kind of bias it has.

As shown by S. Lindberg in [40], there is no ideal routine. What has been used in previous software is the so-called neighbour routine, and this is what has been implemented in land02 within this work. There is definitely room for improvements in terms of the routine, such as using the bunch routine [40], or even smarter guessing routines based on probabilities (like for e.g. the neutron tracker [41]).

The neighbour-routine takes, as its name indicates, the neighbours of the crystal which has been hit[6)] into account. Addback is performed on the transition between SYNC and DHIT levels, thus it is working with calibrated energies in MeV, but determines the energies of clusters of crystals from energies detected in single crystals.

The routine works as follows for each event: the total list of crystals with an energy deposit is retrieved and sorted such that the crystal with the highest energy is placed

[6] This is only completely true for the crystal with the highest energy deposit. The following description of the routine will make that clear.

first, and the one with the lowest is last. This has the simple reason that the routine should also define the crystal which has been hit first, which is needed for Doppler correction. The time resolution of the detector is insufficient for that, but as simulations [40] have shown, over 98% for both protons and γ-photons, with energies of interest to us, hitting in the center of a crystal also deposit most energy in the first crystal. This decreases for both protons and γ-photons, in the case when they hit the edge of a crystal, but is still the best guess in the energy ranges in question.

Subsequently the routine, as long as there are entries in the list, takes the first remaining entry, and defines from that the time and the first crystal which has been hit for the cluster[7)]. It also takes the energy deposited in the crystal, which is then removed from the list. The number of crystals in the cluster is set to one. The cluster multiplicity (i.e. the amount of clusters found for this event) is incremented by 1. Then the routine goes through the remaining list and checks if any neighbour of the primary crystal is listed. If so, and the hit occurs during the predefined time window of 30 ns around the first hit, it adds the energy deposited to the cluster energy and increases the amount of crystals in the cluster by one. The crystal is then removed from the list. The search for neighbours is continued until no more neighbours of the primary crystal are found in the list. Then the cluster is closed and stored. If there are entries left in the list, again the first one is picked as cluster centre and the procedure repeats. This is illustrated in Fig. 5.13.

There are two steps that should be described in more detail. The retrieval of the energy deposited in each crystal and the sorting are nontrivial, since about 60 crystals in the forward direction have a double read-out for proton measurements. In order not to introduce non-smooth behavior due to a sudden transition from the low-gain range (HEB, high energy branch) to the high-gain range (LEB, Low-Energy-Branch), in the range between 30% and 80% of the Low-Energy-Branch, the energy from both branches is averaged. The averaging is done with a weighted average corresponding to the fraction of the detected energy compared to the full range of the LEB. This is illustrated in Fig. 5.14. The other nontrivial point is the handling of overflows. Clusters caused by protons or neutrons might extend to the region where the detector does

[7] The cluster is the group of neighbouring crystals being hit, on which addback to one event will be done.

not have a double read-out and the energy deposits might lead to overflows in these crystals. Nevertheless, the lower limit of the energy might be a valuable information. Therefore, when the overflow bit-mask is set (either for both, or for the one which has only one read-out) the energy in this crystal is set to maximum of the range of that crystal, and a flag is set in order to transfer the overflow information. If such an energy is then added to a cluster, the overflow flag of this cluster is set such that this information is not lost. In this way the user can decide what to do with the information. Often only a minimum energy is required (in order to identify a proton or a neutron), but when extracting γ-spectra, minimum energies are unwanted and can thus be excluded. The diversity in which the information will be processed is also the reason why the algorithm does not discriminate between γ-photons and massive particles.

This might be the place where Doppler-correction is expected. As just explained the discrimination between γ-photons, neutrons and protons has not yet been done. This is in principle possible when using the SST array around the target. Since that implies combination of information from several detectors this belongs to the tracking stage, and is therefore also done using RALF'S TRACKER, see Ref. [34]. The present experiment did unfortunately not feature working box-detectors in the SST-array, and thus the discrimination is not possible in the usual way. What the tracker does instead, is offering a Doppler-corrected energy for each cluster, leaving it to the user to discriminate between protons (neutrons) and γ-photons.

5.4 Difference between addback events and no-addback events in XB

Another recurring question is whether addback affects the determined energy, i.e. broadens or shifts energy peaks. This is studied with data from ^{22}Na source runs performed during the S393 experiment. The widths and peak positions are compared for three different scenarios:

- (calibrated) spectrum with the “neighbour clean” condition,

nominal peak position [keV]	σ singles [keV]	σ pairs [keV]	σ triples [keV]
511	27±2	29±2	33±5
1274	45±1	46±2	49±6

Table 5.1: Averages of the peak widths for single crystal hits, pair hits and triple crystal hits, for both peaks from ^{22}Na, i.e. at 511 keV and at 1274 keV.

- (calibrated) energy sum spectrum of the energy where two neighbouring crystals detected something while their other neighbours did not see anything, i.e. a clean two-neighbour addback,
- (calibrated) energy sum spectrum from three crystals with a common corner that all detected energy deposits but their other neighbours did not, i.e. clean three-crystals addback.

The peaks are fitted using a Gaussian on a linear background[8)] The data have been calibrated using singles spectra extracted with the neighbour clean condition from a different source-run. As can be seen from Table 5.1, the widths show a very slight trend of broadening with the amount of addback-crystals, though the trend is inside the error bars. The peak-positions, though, show a significant trend. As illustrated in Fig. 5.15 the average peak-position is smaller by 20 keV when comparing two-crystal-addback data to single crystal data and is additional 20 keV smaller when comparing three-crystal-addback data to two-crystal-addback data. This is the case for both the 511 keV and the 1274 keV lines.

The constant offset can be explained. As GEANT3 simulations have shown [42], the amount of Compton scatterings per crystal is not constant for the different addback situations. γ-photons depositing the full energy in only one crystal interact with electrons on average 2 to 3 times (depending on the energy, between 0.5 and 2 MeV). γ-photons depositing the full energy in 2 crystals scatter with 3 and 3.9 electrons on average for 0.5 and 2 MeV γ-photons, respectively. γ-photons depositing the full energy in 3 crystals scatter with 3.4 and 4.8 electrons on average, respectively. Selecting events whose full energy has been detected in 1, 2 or 3 crystals thus im-

[8] This simplistic background might affect positions and widths but does that in a systematic way, which might affect the absolute numbers, but not the relative comparison.

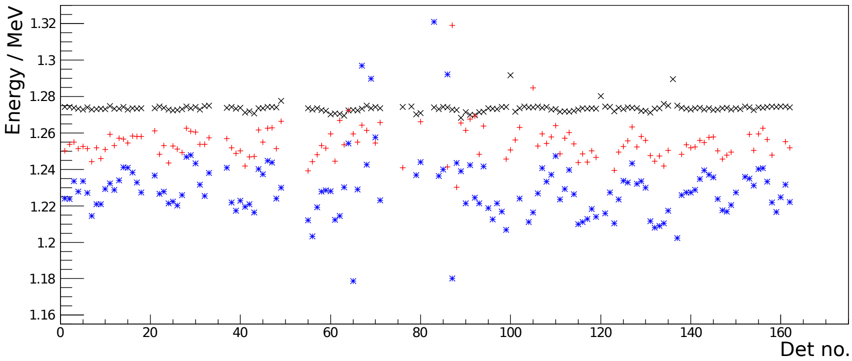

Figure 5.15: Plot of peak position in MeV versus channel number for the three different levels of addback for the 1274 keV peak from ^{22}Na. Crosses (black) indicate the positions of the singles peaks, pluses (red) indicate the peak positions extracted from addback pairs, and stars (blue) indicate the peak positions extracted from addback triples. The latter two values are obtained by averaging over all combinations in which the channel in question is involved.

plicitely selects events for which different numbers of Compton scatterings occurred during the detection process. Since the crystals are calibrated with spectra from single crystals (i.e. themselves), the calibration assumes (depending on energy) 2 to 3 electron collisions. When depositing energy in two crystals, each crystal expects 2 to 3 electrons on average, yielding in total 4 to 6 expected electron collisions. But in fact only 3 to 3.8 scatterings have occurred on average (in both crystals together). As explained by Knoll [43] and Mengesha [44], the amount of scintillation photons created (per MeV) in the crystals depends on the energy of the excited electron. Thus, exciting fewer electrons than expected for a particular energy in crystals causes a different amount of photons being created relative the expected amount. Therefore the calibration is not correct for such events and thus the detected energy is wrongly attributed. This causes the systematic lack of about 20 keV, when the number of crystals hit is increased by one.

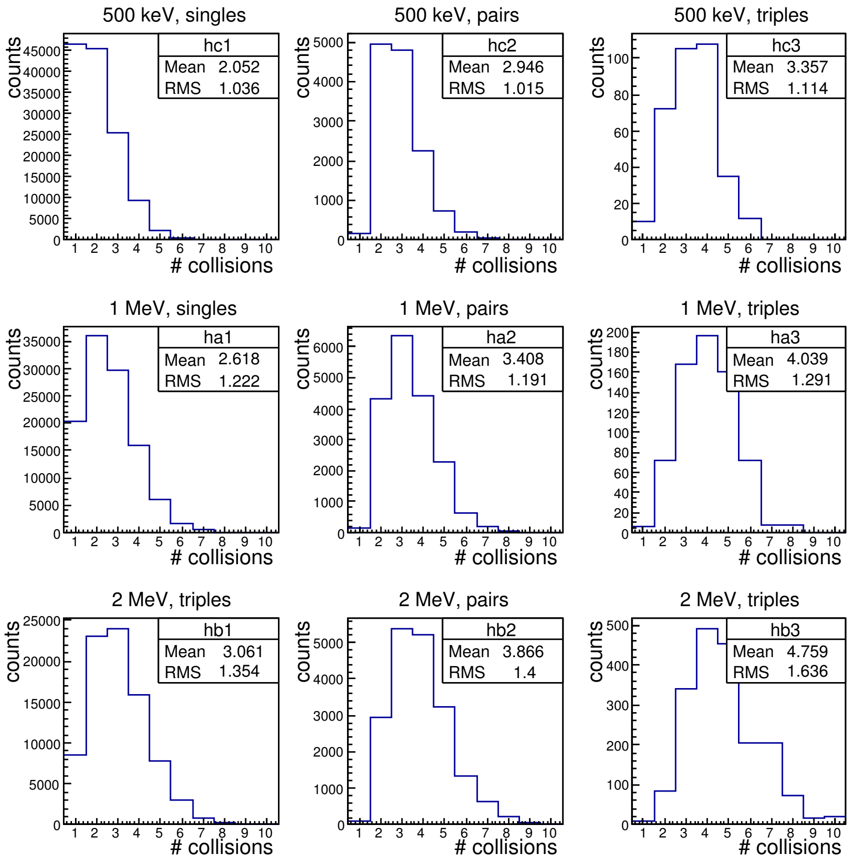

Figure 5.16: Amounts of Compton scatterings for the three different addback situations: singles, pairs and triples (left to right) at the energies 0.5 MeV, 1 MeV and 2 MeV (top to bottom). Simulated in GEANT3 by H.T. Johansson [42].

5.5 Developing the cosmic muon generator for ggland

As motivated in Ref. [36], it is necessary to perform a simulation with a realistic muon distribution in order to be able to perform an energy calibration of the high energy branch in the Crystal Ball taking care of systematic effects. Though codes exist to simulate high-energy muons at underground experiments [45, 46], as well as codes which propagate secondary cosmic rays from the top of the atmosphere down to sea level [47], it was not possible to find an event generator which generated a realistic muon distribution at sea level, down to required energies.
Therefore, a parametrization of muon intensity at sea level by Kempa et al. [48, 49] was used to develop an event generator within the GGLAND framework. GGLAND is a wrapper to GEANT3 and GEANT4, developed by H.T. Johansson in order to enable command-line interface simulations. Most programming needed for the cosmic muon generator has been done by H.T. Johansson, though testing and cross checks were performed by the author. More details on GGLAND can be found in Ref. [50].
The parametrization of the muon distribution is based on measured intensities and depends both on zenith angle and energy. It is valid in the momentum range from 200 MeV/c to 100 GeV/c and at angles between 0° and 88° from the zenith. The randomization according to the intensity distribution is done using a generic 2D function randomizer (written for this application) which is described in the following subsection. The muon charge ratio is also taken into account and as described in Sec. 5.5.2

5.5.1 Randomizing a 2D function in ggland

The general randomization in GGLAND is developed in analogy with the 1D randomizer class *TRandom* in ROOT [32]. The following section describes its working principle.
First the randomization of a function $f(x,y)$ needs to be initialized, then random values according to that function can be extracted. The initialization treats the function such that it is quick to retrieve random values later.
The first step of the initialization is to divide the variable space which is defined or

requested into (2D) intervals. The function is approximated as a quadratic function in each interval. For each interval it is checked whether the integral of the quadratic function equals the integral of the function to be approximated within the given accuracy. If this is the case, the interval is left at its size, if not the interval is divided and new quadratic functions are used for approximation. Once the approximations in all intervals converge, the integral of each interval is calculated (using the quadratic functions) and the sum is normalized, such that the cumulative integral over the entire region of interest is 1. The intervals are then ordered such that the cumulative integral of box 0 to current box is as close to a linear function as possible, see Fig. 5.17b. This makes the later-needed search algorithm faster. Thus, for box n holds:

$$\int_{x_1}^{x_2} F(x)dx = b - a, \tag{5.1}$$

$$F(x) = \int_{y_1}^{y_2} f(x,y)dy, \tag{5.2}$$

where a and b are the cumulative integral at the beginning and the end point of the interval and $[x_1,x_2]$ and $[y_1,y_2]$ define the interval. This is what is needed for initialization.

In order to retrieve a pair of random values (l_x,l_y) according to the distribution function $f(x,y)$, two random numbers (r_1 and r_2) are needed for each pair of random values to be generated. The first random value, r_1, is used to find l_x: This is done by finding the box in which the cumulative integral reaches r_1 (see Fig. 5.17c), and then finding the point l_x at which the cumulative integral equals r_1:

$$\int_{x_1}^{l_x} F(x)dx = r_1 - a. \tag{5.3}$$

With l_x defined, and thus the interval, r_2 is used to find l_y by

$$\frac{\int_{y_1}^{l_y} f(x,y)dy}{\int_{y_1}^{y_2} f(x,y)dy} = r_2. \tag{5.4}$$

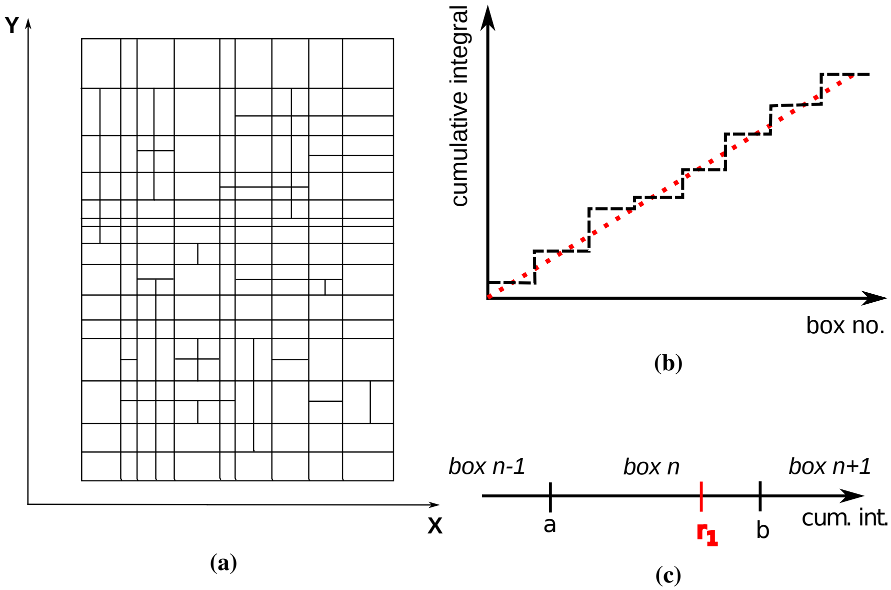

Figure 5.17: Sketches to illustrate the randomization procedure. (a) Displays a possible division into variable intervals in the sampling region. (b) Illustration of the desired order of intervals. (c) Illustrates how a random value is used to retrieve a random value according to the distribution.

In both cases r_1 and r_2 are solved for by inverting the approximative quadratic function. With this method, any reasonably smooth 2D function can be used as a probability distribution to generate pairs of random values.

5.5.2 Creating a realistic muon distribution at sea level

The previous section describes how a function of two variables is treated in GGLAND in order to generate pairs of random values according to that function. This is used to retrieve the absolute momentum and angle with respect to the zenith[9)] for the muon which is to be generated. The angular distribution around the zenith angle, called east-west effect [51], strongly depends on the Earth magnetic field and therefore on the location of the detector. But it is only a perturbation (14% maximum deviation measured at Super-Kamiokande [51]) and has not been measured at the position of GSI. Therefore, the angular distribution around the zenith angle is taken to be isotropic and can easily be randomized.

Another property which has to be sampled is the charge of the muon. The charge ratio depends on the muon momentum at low momenta but seems to flatten out at to a constant ratio at higher momenta [51]. Thus, at muon momenta below 4.16 GeV/c the dependence is assumed to be linear using an interpolation of data measured in [52] and at larger momenta than 4.16 GeV/c the ratio given by the PDG[10)] [51] is used. Since the muon momentum is determined in the first step, determination of the charge is straightforward with a random number and the (momentum dependent) charge ratio.

Finally, the origin of the muon needs to be generated. The distribution used describes the distribution in one point, but the full volume of interest has to see a correct distribution. In order to render a correct distribution in the volume of interest, the user can define the radius of a half-sphere inside which the distribution will be correct. This is realized as described in the following, see Fig. 5.18a for illustration. From the origin of the half-sphere the algorithm traces back anti-parallel to the determined direction of the muon to the surface of the sphere. At that point on the shell, a tangential disk

9) Zenith denotes the upwards direction, and is in the coordinate system of the cave the y-direction.

10) The muon charge ratio (amount of μ^+ divided by amount of μ^-) is given by the PDG, [51], to 1.2766.

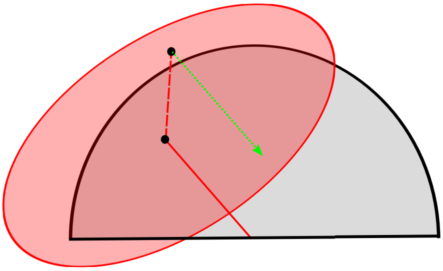

(a) Illustration of the origin randomization of the generated muons. See text for details.

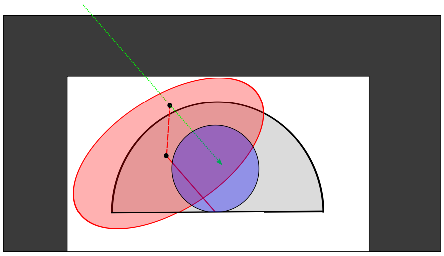

(b) Illustration of the option to shoot from the world edge for the generated muons. See text for details.

of the same radius as the half sphere is considered, and a random point on this disk is chosen as origin. This is done by an uniform distribution of the angle and the square root distribution of the radius, in order to have a uniform distribution of points chosen on the disk. This mechanism ensures that one does not introduce any edge effects or similar in the region of interest. As a measure to allow for a faster simulation and inclusion of large artifacts, for example concrete walls surrounding the detector, an option was designed to back-trace muons (in a straight line) from the generated point anti-parallel to the momentum direction to the edge of the world volume[11)] and to initialize them from there. See illustration in Fig. 5.18b. The distribution of muons is thus only correct inside the specified volume of interest, but traverses (and interacts with) the surrounding material. This option has to be handled with care. If the muons of interest are those which are scattered by the setup, the whole setup should be inside the volume of interest. Though, if only "direct" muons, which are affected only slightly by the setup are of interest, e.g. to test the behavior of a certain detector, this is a reasonable approximation, speeding up simulation time significantly.

5.5.3 Verification of the distribution

The simulations of muons in the Crystal Ball were performed by generating muons with momenta between 1 GeV/c (smaller energies are stopped in the concrete of the cave walls) and $5 \cdot 10^4$ GeV/c (upper end of validity of the simulation) at angles be-

[11)] The world volume in simulations is the term for the total volume simulated.

tween 0 and 88 degrees from the zenith (both limits of the simulation). A model of the concrete walls of Cave C with a thickness of 2.4 m was also simulated[12)] using the option to initialize the muons at the world volume borders. An iron block to mimic the ALADiN magnet was tested, but did not introduce detectable changes in the data.
As the Crystal Ball with its segmentation is a detector suitable to compare the simulated data with recorded data for observables like count-rates or distributions, it provides a good check before analyzing the energy spectra. Since the deposited energy is the observable which should be extracted, cross checks can be done only by using other information, e.g. the distribution of the amount of recorded data over the whole detector does not depend on the deposited energy. Comparison with two different sets of experimental data is shown (data from experiments S393 and S412). The data from the experiments is shown in Fig. 5.19.
In order to see systematic differences, the count rate distributions are displayed in 3D plots, counts (per crystal) vs. θ-angle vs. ϕ-angle. Results from the simulation are displayed in Fig. 5.20a. The left hand plot displays the statistics for grazing events and the right hand plot presents the statistics for opposite events, see Sec. 4.5. The grazing events can be seen to be more frequent in horizontally oriented crystals and the opposite events are more frequent for vertically aligned crystals. This is in perfect agreement with the distribution of cosmic muons, but contradicts what has been measured in the S393 experiment, as shown in Fig. 5.19a. The measured data from S393 displays a big difference between those crystals which are located around the beam pipe and all other crystals for grazing events. For opposite events, the general pattern agrees, but there is a bias towards crystals in the backwards half, which can also be seen for grazing events. Since the muon distribution is a measured one, something in the experimental set-up must cause the bias. This can be identified to be the trigger. The off-spill muon trigger in S393 required both the left and right half of the Crystal Ball to see a high energy deposit which was determined by a LED (Leading Edge Discriminator) for the sum of the energy signal of 16 crystals. Since the crystals were cabled to avoid cross-talk, the threshold of the LED could not be adjusted to the

[12)] This is just a mimic as some parts of the concrete walls actually are thinner than 2.4 m, as well as there is more concrete (not the wall) in the direction of the FRS and also in the direction of other caves.

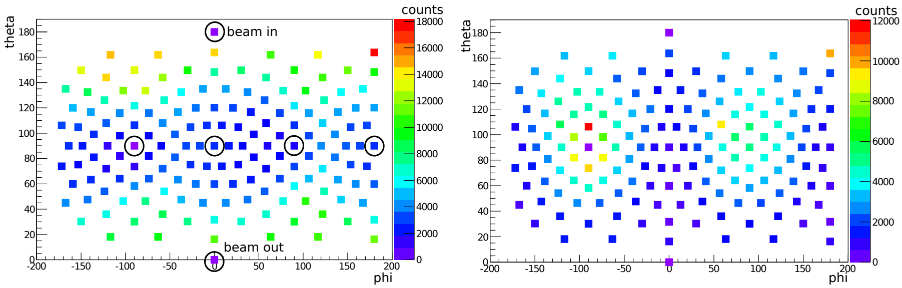

(a) Distribution from the S393 experiment data.

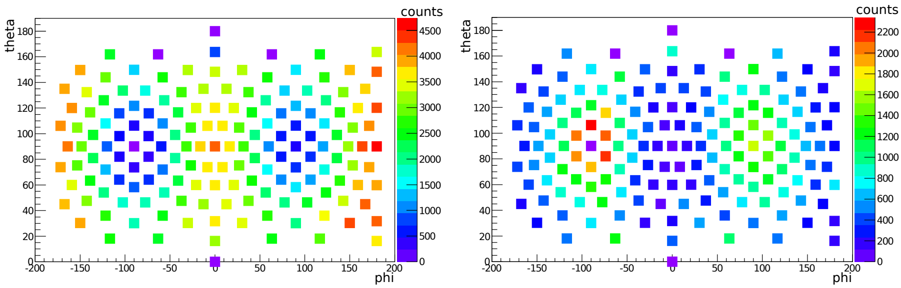

(b) Distribution from the S412 experiment data.

Figure 5.19: Distribution of events usable for energy calibration. Data from two different experiments with different cabling and triggers. Each crystal is represented by a square. The encircled crystals without labels are, from left to right: the bottom crystal (missing), the rightmost crystal, the top crystal, the leftmost crystal. The left plot shows gracing events and the right one opposite events. Compare to simulations shown in Fig. 5.20. For details see text.

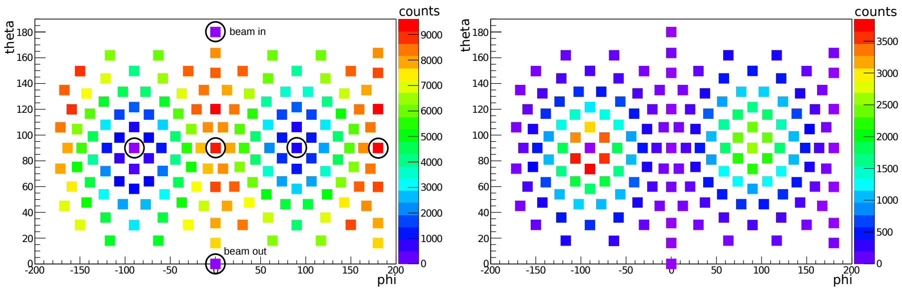

(a) Simulation results without trigger bias.

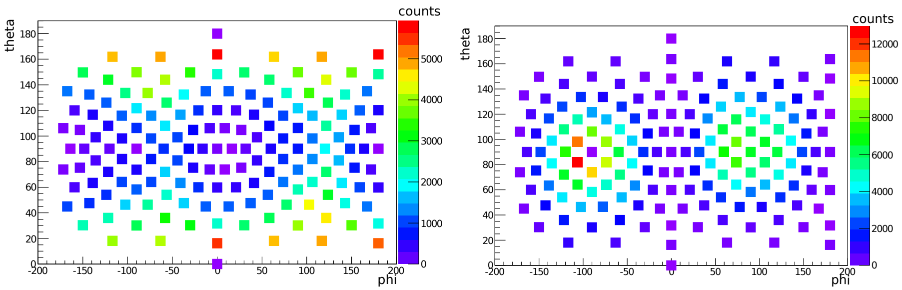

(b) Simulation result employing the S393 trigger mimic.

Figure 5.20: Results from the simulation. The distribution of events used for energy calibration are shown. Each crystal is represented by a square. The encircled crystals without labels are, from left to right: the bottom crystal (missing), the rightmost crystal, the top crystal, the leftmost crystal. The left plot shows gracing events and the right one opposite events. For details see text.

different gains of the different crystals. This therefore causes a bias for the crystals in the backwards direction whose PMTs have a higher gain[13)], and affects the grazing in such a way that only chains which reach over both halves of the detector (or are in random coincidence) are triggered on. The opposite events are not affected by the left and right half trigger, as opposite crystals lie by definition in different halves. This explanation is supported by Fig. 5.20b which displays the simulated results requiring a minimum of 5 MeV deposited in both halves of the Crystal Ball. This Figure is in good agreement with the data obtained during S393, except for the backwards bias. It has not been attempted to include the bias into the simulation. Instead, one can look at data from a different experiment, S412, using a different cabling of the read-out and the high voltage distribution, as well as a different trigger. In that experiment, clusters of neighbouring crystals, facing approximately in the same direction, were read out by one MSCF module and the LED could therefore be adjusted to the gain. Also, left and right half were not discriminated, but the requirement was that two clusters were above threshold. The results of that measurement are shown in Fig. 5.19b, and agree very well with the unbiased simulation results (see Fig. 5.20a), showing that eliminating the set-up bias renders the simulation to reproduce the measurements nicely. On the other hand, it is also possible to mimic the bias of the experimental set-up and reproduce these results.

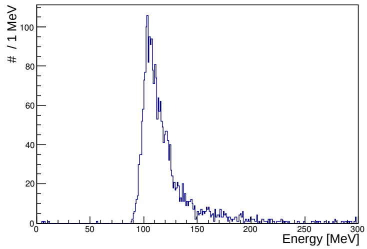

Figure 5.21: Plot showing a typical energy histogram of one crystal for opposite events. Here the energy deposited in crystal 36 is displayed with a requirement that only the exact opposite is hit.

With the conclusion that the simulation is working, and does reproduce measured data, the next step is to analyze the simulated data. The analysis should yield the expected energy deposit and the most probable events each crystal (e.g. the typical

[13)]The gain of the PMTs is adjusted to match the range of the ADC. Since the Doppler boosting is significant at the energies of the experiment, the crystals in backwards direction have a higher gain than the ones in forward direction.

length of the grazing chain). This allows to determine which events are suitable for calibration. An example for an energy spectrum is shown in Fig. 5.21. Further work on the analysis is ongoing.

6 Analysis

6.1 Reaction identification

Since the set-up measures complete kinematics on an event-by-event basis, each event can be analyzed independent of the other events and all reaction products should be detected[1)]. This section describes the different steps how to identify the reaction

$$^{17}\mathrm{C} + p \rightarrow (^{15}\mathrm{B} + n) + p + p. \tag{6.1}$$

Detecting incoming ^{17}C outgoing ^{15}B and a neutron (as ^{16}B is neutron-unbound [11, 12]) is sufficient to identify the reaction uniquely. It is possible to focus on a "cleaner" reaction; quasi-free (p,2p) scattering in the target. In order to identify this, additionally two protons should be detected: the target proton and the proton knocked out from ^{17}C. The identification of such reactions will be described in the last part of this section.

6.1.1 Incoming beam and outgoing fragment identification

Using the track level of LAND02, the identification of the incoming beam using the ID plots of mass vs. mass-over-charge-ratio is straightforward, as displayed in Fig. 6.1. The distribution around the expected position of ^{17}C was fitted with a two-dimensional Gaussian distribution, and a 3σ range around the mean identified as ^{17}C (indicated by the red ellipse in Fig. 6.1). The average kinetic energy of the incoming ^{17}C ions was 437 AMeV and 466 AMeV for the separator settings 5 and 6 respectively.

[1] Due to efficiency and an angular coverage less than 4π, some are lost.

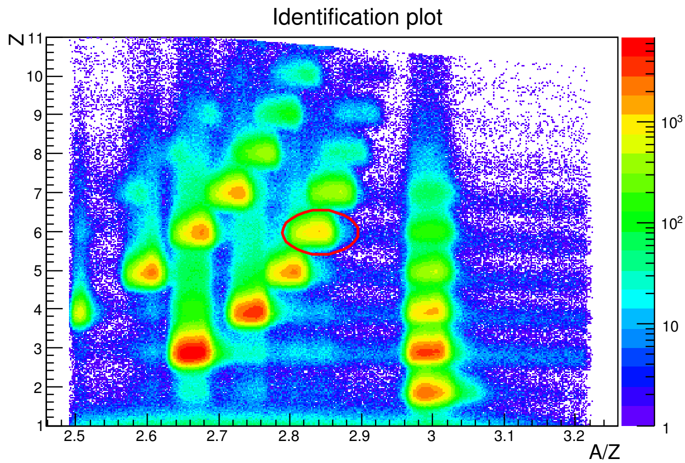

Figure 6.1: Identification plot of the incoming beam for one of the two employed FRS settings (setting 5). The cut used to identify ^{17}C is indicated by the red ellipse.

The next step is the identification of the reaction channel, characterized by proton knock-out from ^{17}C. First of all the fragment has to be identified. The charge of the fragment is determined using the closest SST detector behind the target and the TFW detector, ensuring that no charge-changing reactions took place between target and ToF detector. In order to do that, the energy deposited in those two detectors is plotted versus each other, as shown in Fig. 6.2, because the energy deposited in a material is proportional to Z^2 (of the ion). With incoming ^{17}C selected the highest intensity accumulation spot is generated by carbon isotopes, and the other accumulation points on the diagonal below by respectively smaller charges. Thus the first one below the carbon accumulation point is generated by boron isotopes. Off-diagonal events indicate that a charge-changing reaction took place between SST detector and TFW detector. The cut is determined by fitting the accumulation spot with a two-dimensional Gaussian and allowing everything within 3σ from the mean, as for the incoming beam.

These two cuts determine that ^{17}C ions are incoming and boron isotopes are outgo-

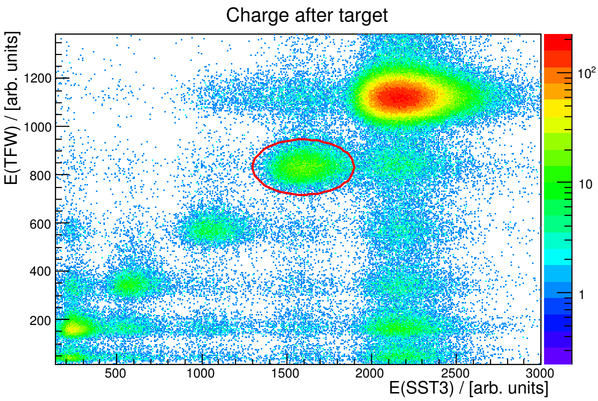

Figure 6.2: Plot of the energy deposited in the TFW vs. the energy deposited in the SST detector directly behind the target, when selecting ^{17}C as incoming beam. The high intensity accumulation point in the upper right corner corresponds to carbon (in both detectors), and the accumulation spot on the diagonal below that one corresponds thus to one charge unit less and therefore boron. The red ellipse indicates the cut used to select boron.

ing, but the mass of the boron isotopes has to be determined by tracking the fragments through the magnet with the help of the TRACKER. After tracking, the mass distribution can be extracted, as seen in Fig. 6.3 for tracked incoming ^{17}C and outgoing boron. Fitting both the $A = 14$ and $A = 15$ peak, the cut was set to be outside the 3σ range of mass 14 and symmetric about the mean of mass 15.

6.1.2 Neutron tracking

Due to the nature of neutrons, several hits even in non-neighbouring paddles of LAND can belong to one neutron. The reconstruction from detected hits to neutrons is done inside LAND02 using the *landshower* algorithm. The algorithm tries to find all causally-linked hits, reconstructing a neutron hit from that. This (as any other reconstruction method using this type of detector) implies that some[2)] events will be

[2] About 18% of one-neutron events are misidentified as two-neutron events, and about 17% of two-neutron events are misidentified as one-neutron events, [53].

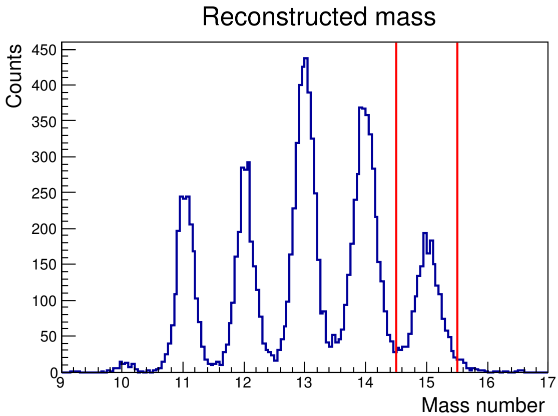

Figure 6.3: Distribution of the mass (in atomic units) after the CH_2 target with incoming ^{17}C and outgoing boron. Red lines indicate the range of the mass cut used to select ^{15}B.

wrongly reconstructed, i.e. that the algorithm reconstructs two neutrons, though only one hit the detector and vice versa. The analysis sometimes allows two neutrons to be reconstructed. The *landshower* algorithm can be optimized for the specific physics case by changing the parameters for identification of causally linked hits, this has not yet been done in this work.

6.1.3 Proton reconstruction

In order to identify a (p,2p) reaction, the two protons emerging from the reaction should be detected. Since this is a relativistic quasi-free scattering (see Ref. [54, 55]), the polar angle (Θ) between the protons lies around 84° at the energies in question. In a fully free, non-relativistic scattering of two protons these have a scattering angle of 90°with respect to each other. The potential leads to forward-focusing as well as the relativistic movement of one of the protons. The protons are emitted back-to-back in the reaction plane, characterized by an azimuthal angle (Φ) of 180°with respect to each other. Therefore two steps need to be taken. Protons have to be identified,

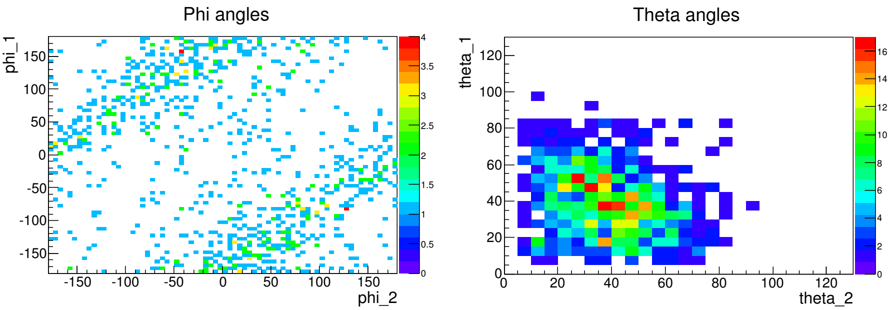

Figure 6.4: Angular correlations of the proton signatures for ^{17}C incoming and ^{15}B outgoing, without requirements on detected neutrons. The left hand panel shows the azimuthal angles and the right hand side the polar angles.

and then the proton multiplicity and their angle in case of multiplicity two has to be determined.

As a first step all clusters with energies above 30 MeV are regarded as protons. Photons should, even with Doppler- boosting, not exceed energies of 30 MeV. If there are exactly 2 proton signatures[3)] detected in the event, the angles with respect to each other are determined. For that the angle of each cluster is randomized inside the crystal which was identified to host the primary hit of the cluster (using the program described in Ref. [37]). Distributions of azimuthal and polar angles for events with two-proton signatures are shown in Fig. 6.4. If the pair fulfills the (p,2p) signature, the event is regarded as (p,2p) event. The conditions used for identifying a (p,2p)-event are i) a polar opening angle between 48° and 120°, and ii) an azimuthal opening angle of 134° to 226°. These conditions seem to be quite lax, but are not. The uncertainty in angle of each crystal is about 7.5° due to the size. This means that an angle inside one crystal module can be approximately 15° off, since there are two crystals, this uncertainty is 30°.

[3] There are a few events with 3 clusters above 30 MeV.

6.2 Experimental conditions

The S393 experiment is a multipurpose experiment with a diverse scope. It aims at studying a large number of light nuclei in complete kinematics. In particular the experiment provides data for studying the cluster structure of Beryllium isotopes, extracting (n,γ) rates for r-process nucleosynthesis, deriving single-particle spectroscopic factors, and studying the shell structure of nuclei near and beyond the neutron dripline.

Data with radioactive beams comprising in total 46 nuclei in the range from $Z = 4$ to $Z = 10$ were studied with six different settings of the FRS. Only two of them (setting 5 and setting 6) provide data on ^{17}C[4].

According to the proposal, setting 5 and 6 should have had 6 and 10 8 h shifts respectively for data taking on the CH_2 target in total, but the total amount of data was taken in 3.38 and 2.25 8 h shifts with CH_2 target and setting 5 and 6 respectively. The cut can be explained by problems in the UNILAC shortening the beam-time by approximately 6 shifts (total requested were 58) but also problems setting up the FRS and re-prioritizing during experiment.

Using the scaler information collected during the experiment it is also possible to check whether the assumed yields were met. The assumed yields, including transmission to the experiment, were not met. The yields were overestimated by a factor 3.8 and 2.8 (for setting 5 and 6) respectively. In total this results in a factor 10.3 less ions of ^{17}C arriving at the experiment compared to the expectations in the proposal. During the experiment in total 713850 incoming ^{17}C ions were measured for both setting 5 and 6.

6.3 Results

The results presented here are without background subtraction and efficiency correction.

As described in the previous section, the experiment delivered limited statistics. Ta-

[4] Additionally setting 4 provides little statistics on ^{17}C but is not close enough in beam energy to allow for a joint analysis.

	no (p,2p) req.	(p,2p) req.
no n cut	1814	405
1 or 2 n	957	269
1 n	878	251

Table 6.1: The table shows the available statistics of ^{17}C incoming and ^{15}B outgoing, regarding neutron and (p,2p) identification.

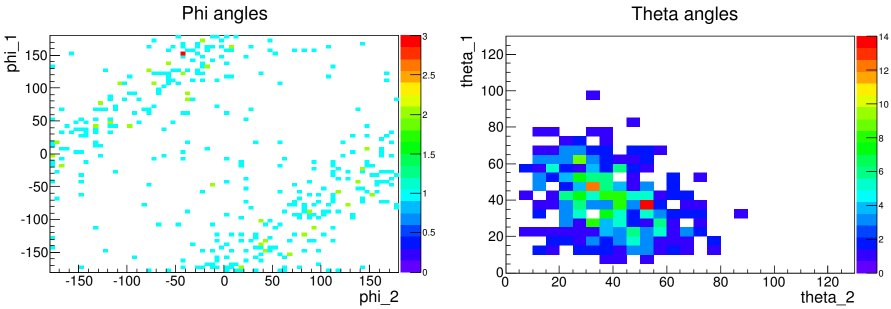

Figure 6.5: Angular correlations of the proton signatures for ^{17}C incoming, ^{15}B outgoing and exactly one neutron reconstructed. The left hand side shows the azimuthal angles and the right hand side the polar angles. Compare to Fig. 6.4, which shows the same plots without requiring a detected neutron.

ble 6.1 summarizes the statistics available for the reaction

$$^{17}\mathrm{C} + p \rightarrow (^{15}\mathrm{B} + n) + p + p. \tag{6.2}$$

for each step of refinement, requiring ^{17}C incoming and ^{15}B outgoing as described above. Without additional cuts around 1800 events are available, while the most stringent conditions reduce the available statistics to only 251 events. A cut on some quantity influences other quantities as well. Requiring the detection of exactly one neutron leads also to a higher fraction of two-proton events that fulfill the (p,2p) conditions. This can be seen by comparing Fig. 6.5 to Fig. 6.4.

6.3.1 Relative Energy

Using the invariant mass approach, it is possible to study the properties of the emitted neutron by constructing the relative energy of fragment (f) and neutron (n). The invariant mass M of a system is defined as

$$\mathscr{M}^2 \cdot c^2 = (\frac{E}{c})^2 - ||\boldsymbol{p}||^2 \tag{6.3}$$

where c is the speed of light and $\boldsymbol{p}$ is the momentum vector. Since the invariant mass is conserved, the excitation energy (E^*) of the fragment after neutron emission can be calculated:

$$E^* = \mathscr{M}_{final} \cdot c^2 - \mathscr{M}_{initial} \cdot c^2. \tag{6.4}$$

The excitation energy can be distributed in two ways: the final fragment is excited and de-excites via emission of a γ-photon, or the energy is converted into relative momentum.

Using Eq. 6.3 and Eq. 6.4 one can express the excitation energy for the fragment + neutron (f+n) case:

$$E^* = \sqrt{M_f^2 + M_n^2 - 2 \cdot \gamma_f \cdot \gamma_n \cdot (1 - \boldsymbol{\beta_f} \cdot \boldsymbol{\beta_n})} - (M_f + M_n) + E_\gamma^f \tag{6.5}$$

where E_γ^f is the energy of the γ-photons as seen in the rest-frame of the fragment. The relative energy is therefore calculated by subtracting E_γ^f:

$$E_{fn} = E^* - E_\gamma^{lab} = \sqrt{M_f^2 + M_n^2 - 2 \cdot \gamma_f \cdot \gamma_n \cdot (1 - \boldsymbol{\beta_f} \cdot \boldsymbol{\beta_n})} - (M_f + M_n) \tag{6.6}$$

with M denoting the mass, $\boldsymbol{\beta}$ being the velocity in units of c and γ denoting the Lorentz factor. A more thorough description can be found in e.g. Ref. [37]. The relative energy spectrum therefore reveals resonances of the unbound system, as these enhance the cross section. Using Breit-Wigner functions, the spectra can be fitted, which allows to determine the orbital angular momentum of the emitted neutron in the ^{16}B.

The relative energy spectrum was extracted employing four different conditions. Ei-

ther “exactly 1 n reconstructed” or “one or two n reconstructed”[5)] was required together with either “no (p,2p) signature required” or “(p,2p) signature required”. The resulting spectra are shown in Fig. 6.6. A peak compatible with the previously measured low-lying state [14, 15, 17] below 100 keV can be seen. Another peak at about 1.1 MeV, which has not been reported so far, is indicated. The state reported by Kalpakchieva *et al.* [14] at 2.32 MeV can probably not be confirmed due to limited statistics in that energy range.
As one can see, the different cuts do not affect the shape of the spectrum. This becomes even clearer from Fig. 6.7, in which the four different histograms are plotted on top of each other and scaled to the same number of counts.

6.3.2 Transverse momentum

The second extracted observable is the transverse momentum of the fragment + neutron system. Nucleons in different orbitals have different momenta, s-wave nucleons have higher momenta than p-, than d-wave nucleons. Therefore, removing one nucleon, and measuring the change in momentum longitudinally or transversally with respect to the beam of the nucleus, yields different distributions for different magnetic quantum numbers.
Since it is not possible to cleanly remove one nucleon, the reaction mechanism plays an important role. The expected momentum distributions depending on the wave function can be calculated and by fitting them to the distribution, the magnetic quantum number of the single-particle-wave-function can be determined[6)].
Traditionally calculations are often done using the Glauber model together with the sudden approximation and either the eikonal optical potential approach, or the Monte-Carlo black disc approach [56]. The sudden approximation states that the interaction is instantaneous, and is valid due to the high beam energies. The eikonal approximation uses a plane wave for the incoming ion, facilitating the description of the nucleus being usually composed of several nuclei [57]. The black disc approximation uses inelastic nucleon-nucleon cross sections assuming independent nucleon-

[5] The first of the two neutrons to arrive in LAND is used for calculating the relative energy.
[6] Or if states are not pure, contributions of the different single-particle-states can be determined.

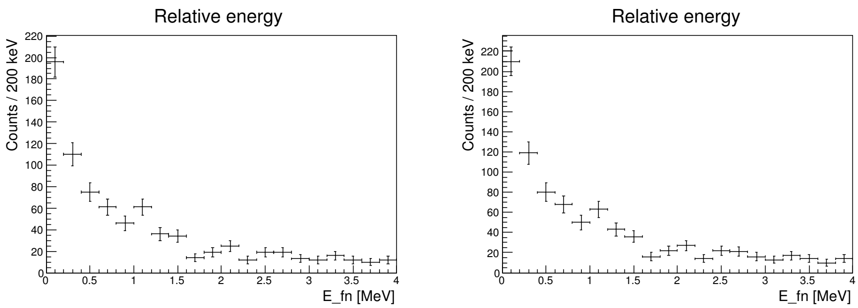

(a) Relative energy with no (p,2p) constraint and exactly one neutron reconstructed.

(b) Relative energy with no (p,2p) constraint and one or two neutrons reconstructed.

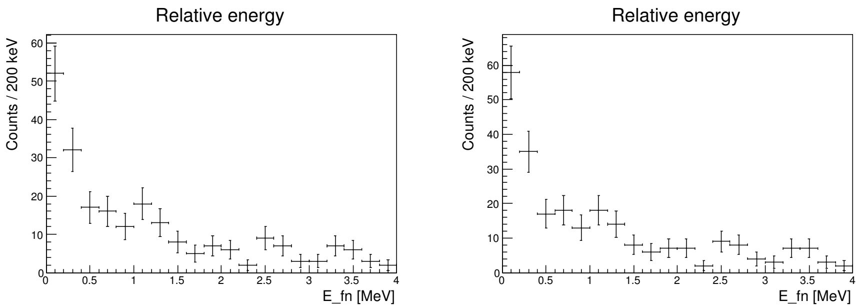

(c) Relative energy with (p,2p) constraint and exactly one neutron reconstructed.

(d) Relative energy with (p,2p) constraint and one or two neutrons reconstructed.

Figure 6.6: Relative energy spectra for the $^{15}B + n$ system for different conditions. The error bars represent statistical errors only.

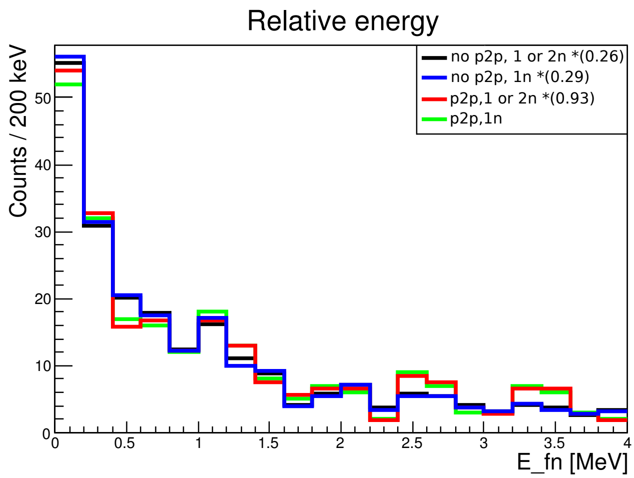

Figure 6.7: Relative energy spectra for the $^{15}B+n$ system. The different conditions are indicated. The histograms (presented in Fig. 6.6) are scaled to hold the same amount of counts.

nucleon collisions and straight trajectories [56].

A recent paper by T. Aumann *et al.* [58] considers quasi-free (p,2p) and (p,pn) reactions on exotic nuclei using eikonal and distorted wave impulse approximation. The latter assumes that only one interaction between the nucleons is dominant. The paper shows that transverse momentum distributions are a suitable tool for probing both core and surface of the nucleus.

Fig. 6.8 shows the reconstructed transverse momenta in case exactly one neutron is reconstructed with and without (p,2p) condition. The data without (p,2p) requirement look quite comparable to data shown by Lecouey *et al.* [15] (c.f. Fig. 1.1).

Additionally the distributions seem to be slightly different for the different cuts. Scaling them to the same amount of statistics, as can be seen in Fig. 6.9, supports that indication. It seems that data fulfilling the (p,2p) requirement results in relatively seen more events at low transverse momenta. The difference could indicate that the (p,2p) reaction has a lower additional momentum transfer than reactions not fulfilling that condition. It could also indicate knock-out from two different single-particle-states

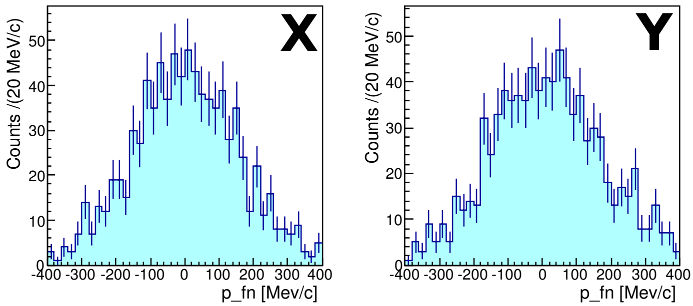

(a) no (p,2p) requirement, exactly one neutron reconstructed

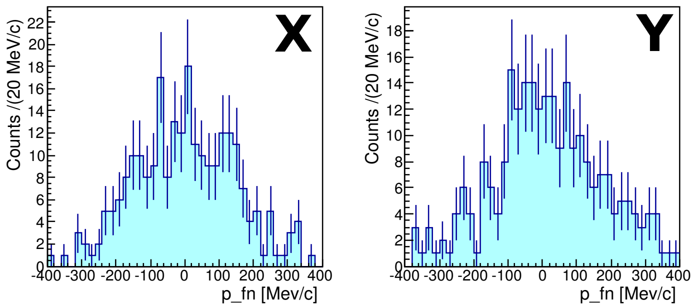

(b) (p,2p) required, exactly one neutron reconstructed

Figure 6.8: Transverse momentum distributions for both transverse directions (see Sec. 2.2.2 for a reminder of the coordinate system). The error bars represent statistical errors only.

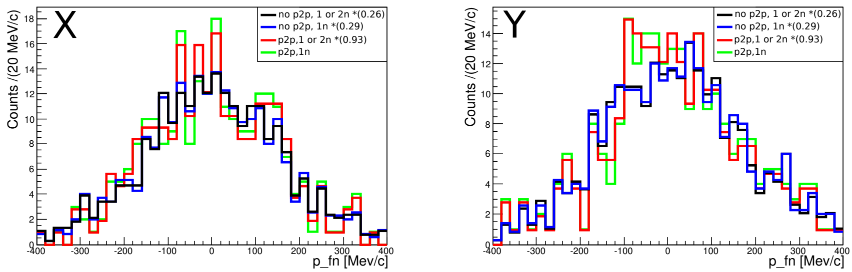

Figure 6.9: Scaled histograms of the transverse momentum of the f+n system for all four conditions.

which have different cross-sections for (p,2p) and non-(p,2p) reactions. The statistics does not allow a definite conclusion at the present state.

6.3.3 Momentum profile

The third physics observable which can be extracted is the momentum profile or profile function. This is the square root of the width of the transverse momentum distribution as a function of relative energy. It conveys information about the angular momentum of the knocked-out proton [59]. The width is determined from the standard deviation according to

$$\sigma = \sqrt{\frac{1}{N-1}\sum_{i}^{N}(p_i - < p >)^2} \tag{6.7}$$

with N denoting the number of data points and p the transverse momentum.
This is compared to the widths calculated as described above, and thus the knock-out of different ℓ-states at different energies can be deduced.
The results are displayed in Fig. 6.10. It is important to note that the limited statistics has a large effect here, because the data are split into the relative energy bins in order to determine the width of the transverse momentum distribution for intervals of relative energy.
Different trends with and without (p,2p) requirement are visible. The (p,2p) events

indicate that there might be protons knocked-out that originate from different single-particle orbitals. This cannot be clearly confirmed or rejected looking at the momentum distributions. The disagreement between x- and y-direction for the non-(p,2p) cases and the large jump of the last data point in the (p,2p) case indicate that the statistical validity needs to be checked.

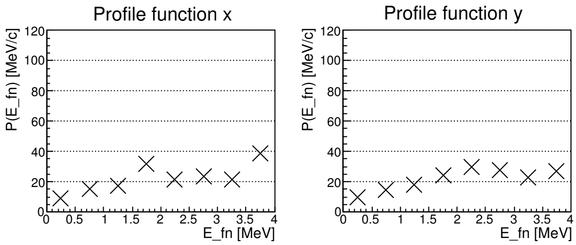

(a) no (p,2p) requirement, one or two neutrons reconstructed

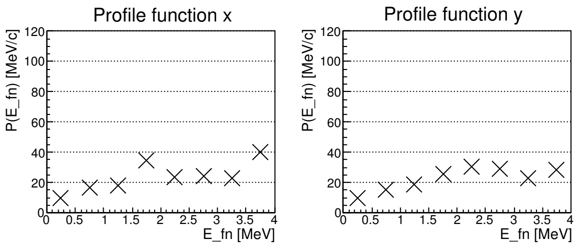

(b) no (p,2p) requirement, exactly one neutron reconstructed

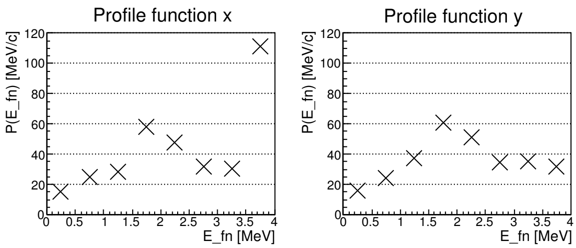

(c) (p,2p) required, one or two neutrons reconstructed

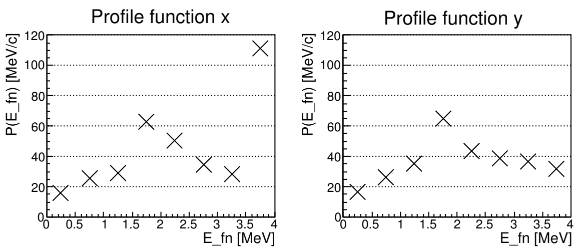

(d) (p,2p) required, exactly one neutron reconstructed

Figure 6.10: Momentum profile of the ^{15}B + n system for the four different conditions. No error bars are shown.

7 Conclusions and Outlook

The data is almost ready for physics interpretation. There are a few things left to be done, like the background subtraction, taking the efficiencies and acceptances into account and normalizing. For the profile function the statistical error needs to be determined, and the experimental uncertainties still lack for all observables. In order to perform the final analysis and physics interpretation, the data need to be fitted. Simulations and calculations of e.g. the transverse momentum distribution will also be necessary.

Due to the limited statistics it might not be possible to perform the full analysis with only H-target[1)]. Instead one could also determine C+CH_2 target observables joining the statistics. Studying the difference between hydrogen and carbon target data will indicate whether such a step is reasonable. This would mean dropping the quasi-free (p,2p) condition, but anyhow the (p,2p) condition seems not to have a considerable impact on the data, though this needs to be examined thoroughly. The reason that there does not seem to be a difference might be caused by the fact that the protons in ^{17}C are deeply bound. Therefore, the condition to knock-out one proton and to detect the ^{15}B +n system might be a sufficient condition for a quasi-free reaction, as other reactions do not allow for a detection of neutron and ^{15}B.

Additionally not all observables have been extracted yet. For example the measured γ-spectrum needs to be retrieved, background subtracted and efficiency corrected. If γ-transitions were observed, the corresponding peaks (and background) need to be fitted. Independent of whether γ-transitions were detected, absolute and, statistics permitting, exclusive cross section will also be derived.

Finally the extracted properties of ^{16}B will be compared to the properties of similar nuclei such as ^{10}Li and ^{13}Be.

[1] Plastic target data removing the C- content using data collected with a C- target.

Furthermore, other reaction channels can be investigated. It would be interesting to look into the $^{17}\mathrm{C} + \mathrm{p} \rightarrow ^{14}\mathrm{B} + \mathrm{n} + \mathrm{n} + \mathrm{p} + \mathrm{p}$ reaction channel, as the amount of ^{14}B produced when requiring one proton removal from ^{17}C is surprisingly high (c.f. Fig. 6.3).
Concerning the developments performed during this work, they were necessary and will be useful in the future for this work and also the analysis of future (and past) LAND/R^{3}B data. The addback routine is crucial both for identifying protons and reconstructing the proper energy of detected γ-photons. The developments concerning the incoming beam, were necessary in order to be able to use all available data, which is very important considering the statistics. The continuous calibration of Crystal Ball is also most important for the reconstruction of the energy of γ-photons. The cosmic muon generator enables a more reliable calibration of Crystal Ball, together with the work presented in Ref. [38].

Glossary

ADC Amplitude-to-Digital-Converter, converts the amplitude of an electric signal into a digital value.

ALADiN "A Large Acceptance DIpole magNet", name of the magnet used to separate ion in the LAND/R^{3}B setup.

CERN European Organization for Nuclear Research, a large research facility for nuclear and particle physics experiments located in Geneva, Switzerland.

CFD Constant-Fraction-Discriminator, produces a logic signal at a certain fraction of the height of a signal, if the signal is above threshold. Used for timing.

CLOCK Program which is part of the LAND02 package, which is used for extracting QDC pedestal values.

DAQ Data AQuisition, can in the wider meaning include all electronic processing of signals coming from detectors, but often refers to the handling and storage of the digital information from detectors (i.e. after processing).

Dead-time The time a detector system (or a whole detector setup) is processing data and not able to process new incoming data is called dead-time.

DTF "Dicke ToF Wand", thick ToF wall, name of the detector used for ToF measurements in the proton arm.

Drip-line The drip-line is the name of the "border" between bound and unbound nuclei. It exists on the proton-rich and on the neutron-rich side, called the proton drip-line and the neutron drip-line respectively.

FAIR Facility for Anti-proton and Ion Research. The international successor facility of GSI under construction at the GSI site.

FRS FRagment Separator, part of the accelerator facility of GSI, used to produce radioactive ions and filter out requested ones.

GEANT Software for simulation of particle interaction with matter, for particles ranging from light quanta to heavy ions. It is developed at CERN.

GFI "Grosser Fiber Detector", big fiber detector, name of the detectors used for position measurements of the fragments behind the magnet.

GGLAND Wrapper software for easy command line interface simulations with GEANT, developed mainly by H.T. Johansson.

GSI Gesellschaft für SchwerIonen forschung, Helmholtz Centre for Heavy Ion Research, situated in Darmstadt, Germany. At this site, the experiments treated in this thesis were performed. It is the precursor facility of FAIR.

ISOL Ion Separation OnLine, a technique for producing radioactive ions.

phase1 Small program which is part of the LAND02 package, which is used for synchronizing detectors internally.

LAND Large Area Neutron Detector. The neutron detector used in the present experiment. Nowadays also used as a name of the experimental setup.

LAND02 Program package originally developed by H.T. Johansson, which is used by the collaboration for calibration and data analysis of the data from the LAND/R^3B setup.

LED here: Leading Edge Discriminator, an electronic module which gives out a logic signals once a pulse is above the defined threshold.

Magic number Magic number is the term for the numbers of protons (neutrons) after which the 2 proton (neutron) separation energy drops sharply. (It otherwise increases with increasing number of protons (neutrons). In the shell model these are the shell closures.

MS Master Start, the (trigger) signal, coming from the central trigger logic, conveying the information to the read-out modules that the event has to be read out.

MSCF Mesytech Spectroscopy amplifier with Constant Fractions, a module used for the XB splitting and amplifying the analog signals, preparing for TDC, ADC and producing trigger signals.

PDC "Proton Drift Chamber", name of the detectors used for position detection behind ALADiN in the proton arm.

Pile-up When two ions are incident onto a detector very close in time (and space), they cannot be separated. Their pulses "pile up" rendering such an event unusable.

PMT PhotoMultiplier Tube, a device that uses the photoelectric effect to produce an electric signal out of the light impinging onto its window, with a high amplification factor. Usually used in combination with a scintillating detector.

POS "POSition detector" name of the detector used for timing measurements before the target. It is not used for position measurements anymore.

PSP "Position Sensitive Pin-diode" name of the detector used for energy detection before the target.

QDC Charge(=Q)-to-Digital-Converter, converting the charge which corresponds to the area of a voltage pulse to a digital value.

QFS Quasi-free scattering, a scattering process of two nuclei in which only part of the nuclei is involved and (directly) affected by the collision.

R^{3}B Reactions with Relativistic Radioactive Beams, the next-generation LAND experiment at FAIR.

ROLU "Rechts-Oben-Links-Unten" name of the veto detector used in the experiment (located before the target).

S2 A focal point in the FRS. The degrader and the SCI1 detector are located there.

S393 Name of the experiment which is analyzed in this work.

S8 Last focal point in the FRS before the experiment. The SCI2 detector is located there.

SCI The name of the two detectors located at the FRS, called SCI1 and SCI2. They are made of sheets of plastic scintillator.

SIS18 SchwerIonen Synchrotron, heavy ion synchrotron, the second stage accelerator at GSI situated between the UNILAC and the FRS.

SST "Silicon Strip Detector" name of the silicon detectors surrounding the target.

TCAL Small program which is part of the LAND02 package, which is used for extracting the gain of a TDC channel using dedicated data.

ToF Time-of-flight, the time it takes for an ion to travel from one place to another (usually between detectors).

Tpat Trigger pattern, a defined combination of raw-triggers gives a certain Tpat.

Trigger Electronic signal starting the conversion and storage of signals arriving at the electronic modules.

TFW "ToF Wand", ToF wall, name of the detector used for ToF detection in the fragment arm.

UNILAC UNIversal Linear ACcelerator, the first acceleration stage at GSI after which the beam can be used for experiments or be further accelerated in the SIS.

XB "Crystal Ball" name of the calorimeter surrounding the target area.

Acknowledgements

This work would not be what it is without the help of several people.
Most importantly "thank you" to my supervisors Thomas Nilsson and Andreas Heinz, complementing each other very well! A big thanks I also owe Håkan Johansson who was collaborator on a few of the development projects, and is always willing to help when programming does not work or something about the experiments is unclear. I would like to thank Ralf Plag for always being quick in response to questions concerning LAND02 or the TRACKER, despite all PhD students in the collaboration nagging at him for help.
Thanks to Björn Jonson for carefully answering any nuclear physics question. All collaborators working at GSI and around, thanks for always welcoming us and appreciating the work we contribute. To all fellow PhD students in the R^3B collaboration: thank you for making experiments, meetings and workshops as fun as they are.
Not to forget, I would like to thank everyone in the department for a nice and fun working environment, especially the PhD students. The magisol collaborators I would like to thank for being able to work on completely different experiments at ISOLDE, CERN. It is always fun, not only because of the physics.
Then there are people contributing in the non-physics domain. I would like to thank my friends, the "öko-clique", from Bremen for still being there, and the "weirdo" people who made me feel welcome in Gothenburg (and thanks for the Swedish training!). Last but not least, thanks to my family and especially Fabian for being my "ground-connection".

Bibliography

[1] J. Magill, G. Pfennig, R. Dreher, and Z. Soti: *Chart of nuclides, 8th edition*. Technical report, Forschungszentrum Karlsruhe in der Helmholtz Gesellschaft, 2013. `http://www.nucleonica.net`.

[2] M. G. Mayer: *On Closed Shells in Nuclei*. Phys. Rev., 74(3):235–239, Aug 1948.

[3] M. G. Mayer: *On Closed Shells in Nuclei. II*. Phys. Rev., 75(12):1969–1970, Jun 1949.

[4] M. G. Mayer: *Nuclear Configurations in the Spin-Orbit Coupling Model. I. Empirical Evidence*. Phys. Rev., 78(1):16–21, Apr 1950.

[5] O. Haxel, J. Hans D. Jensen, and H. E. Suess: *On the "magic numbers" in nuclear structure*. Phys. Rev., 75:1766–1766, Jun 1949. `http://link.aps.org/doi/10.1103/PhysRev.75.1766.2`.

[6] E. Caurier, G. Martinez-Pinedo, F. Nowacki, A. Poves, and A. P. Zuker: *The shell model as a unified view of nuclear structure*. REVIEWS OF MODERN PHYSICS, 77(2):427–488, PRAPR 2005, ISSN 0034-6861.

[7] L. Coraggio, A. Covello, A. Gargano, N. Itaco, and T. T. S. Kuo: *Shell-model calculations and realistic effective interactions*. In Faesssler, A (editor): *PROGRESS IN PARTICLE AND NUCLEAR PHYSICS, VOL 62, NO 1*, volume 62 of *Progress in Particle and Nuclear Physics*, pages 135–182. 2009.

[8] K. Riisager: *Halos and related structures*. Physica Scripta, 2013(T152):014001, 2013. `http://stacks.iop.org/1402-4896/2013/i=T152/a=014001`.

[9] H. Simon: *Halo nuclei, stepping stones across the drip-lines*. Physica Scripta, 2013(T152):014024, 2013. `http://stacks.iop.org/1402-4896/2013/i=T152/a=014024`.

[10] R. Kanungo: *A new view of nuclear shells*. Physica Scripta, 2013(T152):014002, 2013. `http://stacks.iop.org/1402-4896/2013/i=T152/a=014002`.

[11] J. D. Bowman, A. M. Poskanzer, R. G. Korteling, and G. W. Butler: *Detection of neutron-excess isotopes of low-z elements produced in high-energy nuclear reactions*. Phys. Rev. C, 9:836–851, Mar 1974. `http://link.aps.org/doi/10.1103/PhysRevC.9.836`.

[12] M. Langevin, E. Quiniou, M. Bernas, J. Galin, J.C. Jacmart, F. Naulin, F. Pougheon, R. Anne, C. Détraz, D. Guerreau, D. Guillemaud-Mueller, and A.C. Mueller: *Production of neutron-rich nuclei at the limits of particles stability by fragmentation of 44* $^{MeV}/_{u}$ ^{40}*Ar projectiles*. Physics Letters B, 150(1–3):71–74, 1985, ISSN 0370-2693. `http://www.sciencedirect.com/science/article/pii/0370269385901406`.

[13] H.G. Bohlen *et al.*: *Study of light neutron-rich nuclei with* ^{14}*C-induced reactions*. Nuclear Physics A, 583(0):775–782, 1995, ISSN 0375-9474. `http://www.sciencedirect.com/science/article/pii/037594749400757E`.

[14] R. Kalpakchieva *et al.*: *Spectroscopy of* ^{13}*B,* ^{14}*B,* ^{15}*B and* ^{16}*B using multi-nucleon transfer reactions*. Eur.Phys.J. A, 7(4):451–461, 2000, ISSN 1434-6001. `http://dx.doi.org/10.1007/PL00013641`.

[15] J.L. Lecouey *et al.*: *Single-Proton Removal Reaction Study of B-16*. Phys.Lett., B672:6–11, 2009.

[16] R.A. Kryger *et al.*: *Upper limit of the lifetime of B-16*. Phys.Rev., C53:1971–1973, 1996.

[17] A. Spyrou *et al.*: *First evidence for a virtual B-18 ground state*. Phys.Lett., B683:129–133, 2010.

[18] E. K. Warburton and B. A. Brown: *Effective interactions for the $p-s-d$ nuclear shell-model space*. Phys. Rev. C, 46:923–944, Sep 1992. http://link.aps.org/doi/10.1103/PhysRevC.46.923.

[19] M. Dufour and P. Descouvemont: *Low-lying resonances in the B-16 nucleus*. Phys.Lett., B696:237–240, 2011.

[20] Y. Blumenfeld, T. Nilsson, and P. Van Duppen: *Facilities and methods for radioactive ion beam production*. Physica Scripta, 2013(T152):014023, 2013. http://stacks.iop.org/1402-4896/2013/i=T152/a=014023.

[21] T. Nilsson. private communication, December 2013.

[22] H. H. Gutbrod, I. Augustin, H. Eickhoff, K. D. Groß, W. F. Henning, D. Krämer, and G. Walter (editors): *FAIR Baseline Technical Report*. GSI, 2006.

[23] R. Plag: *land02 - featuring the unofficial guide to the unofficial version of land02*. http://web-docs.gsi.de/%07Erplag/land02/.

[24] S. Lindberg: *Private Communication*.

[25] V. Panin: *Fully exclusive Measurements of Quasi-Free Single-Nucleon Knockout Reactions in Inverse Kinematics*. PhD thesis, TU Darmstadt, 2012.

[26] V. Metag, R.D. Fischer, W. Kühn, R. Mühlhans, R. Novotny, D. Habs, U.v. Helmholt, H.W. Heyng, R. Kroth, D. Pelte, D. Schwalm, W. Hennerici, H.J. Hennrich, G. Himmerle, E. Jaeschke, R. Repnow, W. Wahl, E. Adelberger, A. Lazzarini, R.S. Simon, R. Albrecht, and B. Kolb: *Physics with 4-π-γ-Detectors*. Nucl.Phys., A409:331c–342c, 1983.

[27] T. Blaich *et al.*: *A Large area detector for high-energy neutrons*. Nucl.Instrum.Meth., A314:136–154, 1992.

[28] K. Mahata, H.T. Johansson, S. Paschalis, H. Simon, and T. Aumann: *Position reconstruction in large-area scintillating fibre detectors*. Nucl.Instrum.Meth., A608:331–335, 2009.

[29] A. Najafi: *Calibration of drift chambers*. R^{3}B Analysis Workshop 2011.

[30] H. T. Johansson: *Hunting Tools Beyond the Driplines*. PhD thesis, Chalmers University of Technology, 2010.

[31] H. T. Johansson: *The DAQ always runs*. Licentiate thesis, Chalmers University of Technology, 2006.

[32] R. Brun and F. Rademakers: *Root – an object oriented data analysis framework*. Nuclear Instruments and Methods in Physics Research Section A: Accelerators, Spectrometers, Detectors and Associated Equipment, 389(1-2):81–86, 1997. `http://www.sciencedirect.com/science/article/B6TJM-3SPKX96-1F/2/3aa2b2cb72c9a4316a842802541bf317`.

[33] PAW Physics Analysis Workstation: *CERN Program Library Long Writeup Q121*. Information Technology Division, CERN, Geneva, Switzerland, 1999.

[34] R. Plag: *Some Documentation on Ralf's tracker*. GSI, 2013. `http://ralfplag.de/tracker`.

[35] D. Rossi: *Dominics calibration scripts*, CVS repository: lx-pool.gsi.de:/u/drossi/.nimocvs/calscript.

[36] R. Thies: *Prototype tests and pilot experiments for the R^{3}B scintillator based detector systems*. Master's thesis, Chalmers University of Technology, 2011.

[37] F. Wamers: *Quasi-free Knockout Reactions with the Proton-dripline Nucleus ^{17}Ne*. PhD thesis, TU Darmstadt, 2011.

[38] S. Lindberg, R. Thies, T. Axelsson, V. Babic, K. Boretzky, A. Charpy, E. Fiori, I. Gasparic, P.M. Hansson, A. Heinz, H.T. Johansson, J.L. Håkansson, Kudelkin N.S., M. Mårtensson, T. Nilsson, R. Plag, N. Rosholm, D. Rossi, H. Simon, F. Strannerdahl, and the R^{3}B collab.: *Proton-Muon Energy Correlation in the Crystal Ball*. GSI scientific report 2012, 2013.

[39] F. James and M. Roos: *Minuit - a system for function minimization and analysis of the parameter errors and correlations*. Computer

Physics Communications, 10(6):343–367, December 1975. `http://www.sciencedirect.com/science/article/B6TJ5-46FPXJ7-2C/2/58a665cfee07e122711a859fef69c955`.

[40] S. Lindberg: *Optimised Use of Detector Systems for Relativistic Radioactive Beams*. Master's thesis, Chalmers University of Technology, 2013.

[41] H. Törnqvist and L. Trulsson: *Probabilistic neutron tracker*. Master's thesis, Chalmers University of Technology, 2009.

[42] H.T. Johansson. private communication, 2012.

[43] G.F. Knoll: *Radiation Detection and Measurement*. John Wiley and sons, 3rd edition, 2000.

[44] W. Mengesha, T.D. Taulbee, B.D. Rooney, and J.D. Valentine: *Light yield non-proportionality of CsI(Tl), CsI(Na), and YAP*. IEEE Transactions on Nuclear Science, 45(3):456–461, 1998.

[45] Hong Ma: *LAr Cosmic Muon Monte Carlo Simulation*. Brookhaven National Laboratory, 2003. `http://www.usatlas.bnl.gov/%07Ehma/Cosmic/CosmicMuonMC.html`.

[46] L. Sonnenschein: *CMS: Cosmic muons in simulation and measured data*. arXiv, 2011.

[47] D. Heck: *CORSIKA an Air Shower Simulation Program*. Karlsruhe Institute of Technology, 2013. `http://www-ik.fzk.de/%07Ecorsika`.

[48] J. Kempa and I.M. Brancus: *Zenith angle distributions of cosmic ray muons*. Nucl.Phys.Proc.Suppl., 122:279–281, 2003.

[49] J. Kempa and A. Krawczynska: *Low energy muons in the cosmic radiation*. Nucl.Phys.Proc.Suppl., 151:299–302, 2006.

[50] H. T. Johansson: *ggland - command-line simulation wrapper*, 2013. `http://fy.chalmers.se/%07Ef96hajo/ggland`.

[51] J. Beringer et al.(Particle Data Group): *24. COSMIC RAYS*. Phys. Rev. D, 2012.

[52] S. Haino, T. Sanuki, K. Abe, K. Anraku, Y. Asaoka, *et al.*: *Measurements of primary and atmospheric cosmic - ray spectra with the BESS-TeV spectrometer*. Phys.Lett., B594:35–46, 2004.

[53] J. Gill and S. Wranne: *Evaluation of neutron tracker algorithms for land and neuland*. Master's thesis, Chalmers tekniska högskola, 2011. 40.

[54] G. Jacob and TH. A. J. Maris: *Quasi-free scattering and nuclear structure*. Rev. Mod. Phys., 38:121–142, Jan 1966.

[55] G. Jacob and TH. A. J. Maris: *Quasi-free scattering and nuclear structure. ii.* Rev. Mod. Phys., 45:6–21, Jan 1973.

[56] M. L. Miller, K. Reygers, S. J. Sanders, and P. Steinberg: *Glauber modeling in high-energy nuclear collisions*. ANNUAL REVIEW OF NUCLEAR AND PARTICLE SCIENCE, 57:205–243, 2007, ISSN 0163-8998.

[57] C.A. Bertulani and P.A. Danielewicz: *Introduction to Nuclear Reactions*. IOP, 2004, ISBN 9780750309325.

[58] T. Aumann, C. A. Bertulani, and J. Ryckebusch: *Quasifree $(p,2p)$ and (p,pn) reactions with unstable nuclei*. Phys. Rev. C, 88:064610, Dec 2013. `http://link.aps.org/doi/10.1103/PhysRevC.88.064610`.

[59] Yu. Aksyutina, T. Aumann, K. Boretzky, M.J.G. Borge, C. Caesar, A. Chatillon, L.V. Chulkov, D. Cortina-Gil, U. Datta Pramanik, H. Emling, H.O.U. Fynbo, H. Geissel, G. Ickert, H.T. Johansson, B. Jonson, R. Kulessa, C. Langer, T. LeBleis, K. Mahata, G. Münzenberg, T. Nilsson, G. Nyman, R. Palit, S. Paschalis, W. Prokopowicz, R. Reifarth, D. Rossi, A. Richter, K. Riisager, G. Schrieder, H. Simon, K. Sümmerer, O. Tengblad, H. Weick, and M.V. Zhukov: *Momentum profile analysis in one-neutron knockout from Borromean nuclei*. Physics Letters B, 718(4–5):1309–1313, 2013, ISSN 0370-2693. `http://www.sciencedirect.com/science/article/pii/S0370269312012816`.